Structural Basis of Mitochondrial Dysfunction in Response to Cytochrome *c* Phosphorylation at position 48

Blas Moreno-Beltrán[1,*], Alejandra Guerra-Castellano[1,*], Antonio Díaz-Quintana[1], Rebecca Del Conte[2], Sofía M. García-Mauriño[1], Sofía Díaz-Moreno[3], Katiuska González-Arzola[1], Carlos Santos-Ocaña[4], Adrián Velázquez-Campoy[5], Miguel A. De la Rosa[1], Paola Turano[2] & Irene Díaz-Moreno[1,#]

[1]Instituto de Investigaciones Químicas, cicCartuja, Universidad de Sevilla – CSIC, Avda. Américo Vespucio 49, 41092 Seville (Spain).

[2]Magnetic Resonance Center (CERM) – Department of Chemistry, University of Florence, Via Luigi Sacconi 6, 50019 Sesto Fiorentino, Florence (Italy).

[3]Diamond Light Source Ltd., Harwell Science and Innovation Campus, Didcot, Oxfordshire OX11 0DE (United Kingdom).

[4]Centro Andaluz de Biología del Desarrollo, Universidad Pablo de Olavide – CSIC, and CIBERER Instituto de Salud Carlos III, Carretera de Utrera km. 1, 41013 Seville (Spain).

[5]Institute of Biocomputation and Physics of Complex Systems (BIFI), Joint Unit BIFI-IQFR (CSIC), Universidad de Zaragoza, Mariano Esquillor s/n, 50018 Zaragoza (Spain).

* These authors contribute equally to this work.

[#] Correspondence should be addressed to I. D.-M. (idiazmoreno@us.es)

Telephone number: +34 954489513; Fax number: +34 954460065

ABSTRACT

Regulation of mitochondrial activity allows cells to adapt to changing conditions and to control oxidative stress, and its dysfunction can lead to hypoxia-dependent pathologies, such as ischemia and cancer. Although cytochrome *c* phosphorylation—in particular, at tyrosine 48—is a key modulator of mitochondrial signaling, its action and molecular basis remain unknown. Here, we mimic phosphorylation of cytochrome *c* by replacing tyrosine 48 with *p*-carboxy-methyl-L-phenylalanine (*p*CMF). The NMR structure of the resulting mutant reveals significant conformational shifts and enhanced dynamics around *p*CMF that could explain changes observed in its functionality: the phosphomimetic mutation impairs cytochrome *c* diffusion between respiratory complexes, enhances hemeprotein peroxidase and ROS scavenging activities and hinders caspase-dependent apoptosis. Our findings provide a framework to further investigate the modulation of mitochondrial activity by phosphorylated cytochrome *c* and to develop novel therapeutic approaches based on its pro-survival effects.

SIGNIFICANCE STATEMENT

Cell response to physiological changes and oxidative stress involves the modulation of mitochondrial metabolism. Its dysfunction favors the development of hypoxia-dependent pathologies, including ischemia and cancer. A key modulator of mitochondrial activity is cytochrome *c*, whose cell function is modulated by tyrosine phosphorylation. However, how such modification affects cytochrome *c* structure and function is barely known. Here, we report that a phosphomimetic mutant of cytochrome *c* exhibits enhanced dynamics, which could be responsible for the observed differences of cytochrome *c* functionality in oxidative stress and cell death. Thus, phosphorylation of cytochrome *c* becomes a target for further development of robust therapeutic approaches.

\body

INTRODUCTION

Oxidative phosphorylation (OxPhos) relies on the electron transport chain (ETC) to generate the membrane potential that drives ATP synthesis (1). Components of the ETC oxidize substrates to reduce molecular oxygen, thereby producing water. Nevertheless, around 2% of the electrons flowing across the ETC yield reactive oxygen species (ROS) (2). ROS are a source of oxidative stress and act as signaling molecules at low concentrations (3-5). Hindering redox reactions within the distinct ETC membrane complexes (complexes I to V) leads to enhanced ROS production (6). The activity of the ETC is tightly regulated by posttranslational modifications of its components, isoform swapping and modulation of the equilibria for the association of the membrane protein complexes into supercomplexes (3, 7). Such associations allow substrate channeling while modulating ROS production (3, 7).

Oxidative stress response involves redox signals modulating protein phosphorylation (8). In the ETC, the major phosphorylation targets are NADH:UQ oxidoreductase, cytochrome *c* (C*c*) and cytochrome *c* oxidase (C*c*O) (9). Besides being essential for oxidative respiration (**Figure 1a**), C*c* acts as a redox regulatory protein within the mitochondrial intermembrane space (10). In addition, C*c* aids to control ROS levels by oxidizing superoxide anions (11) and exhibiting peroxidase activity (12); the latter, however, also yields lipid peroxidation (13, 14). Furthermore, C*c* plays a crucial role in programmed cell death, a process that is only in partially understood (15-21). In this context, a fraction of C*c* binds and oxidizes cardiolipin (CL) at the internal mitochondrial membrane, thereby facilitating the release of unbound C*c* to the cytoplasm (16, 17). In mammalian cells, extramitochondrial C*c* interacts with apoptosis activating factor-1 (Apaf-1) in the cytoplasm to spark the caspase proteolytic cascade (15). It has recently been shown that C*c* can interact with several other proteins outside the mitochondria in humans and plants (18-21). The similarities between the C*c* signaling networks in both

organisms suggest that key programmed cell death pathways are conserved along evolution (22).

C*c* phosphorylation is an alleged modulator of the mitochondrial cell death pathway (23, 24). Its deregulation is believed to be related to the onset of neurological disorders and cancer (24). Phosphorylation of C*c* is easily reversed by phosphatases, hampering the isolation of the modified protein from tissues (25). Tyr-to-Glu substitutions of C*c*, designed to emulate Tyr48 phosphorylation, impair both the electron donation to C*c*O and the activation of caspase-9 mediated by Apaf-1 *in vitro* (26, 27). Notably, nitration of this residue also hinders the ability of C*c* to activate Apaf-1 (28-30). Thus, these posttranslational modifications alter both mitochondrial and cytoplasmic functions of C*c*. Tyr48 phosphorylation also affects the physical-chemical properties of C*c*, such as its alkaline transition and midpoint reduction potential (E_0) (27, 31). Understanding the origin of these effects and how they affect C*c* activities requires to solve the 3D conformation of the phosphorylated species. However, deciphering the effects of Tyr48 phosphorylation on the structure and dynamics of C*c* is highly challenging because its reactivity towards phosphatases. Indeed, no atomic resolution structure has been reported for either phosphorylated C*c* or any reliable mimic mutant.

Here, we have elucidated the structure of a phosphomimetic C*c* variant in which Tyr48 is replaced by the synthetic, non-canonical amino-acid *p*-carboxy-methyl-L-phenylalanine (*p*CMF). We show that such replacement induce local perturbations of the C*c* structure and enhanced internal dynamics of the mutation surroundings. We used biochemical assays to show that the Y48*p*CMF mutation impairs C*c* channeling between cytochrome bc_1 (Cbc_1) and C*c*O, enhances the peroxidase activity and induces an anti-apoptotic function of C*c*.

RESULTS

Phosphorylation of Tyr48 induces local structural changes in cytochrome *c*

To understand how phosphorylation affects the structure of human C*c*, we tackled the challenge of fully characterizing the phosphomimetic mutant Y48*p*CMF C*c* in its reduced form, which is the redox state of C*c* donating electrons to C*c*O in homeostasis and is essential for its apoptotic activity, since C*c* becomes highly reduced upon its release from the mitochondria to the cytosol (32). Y48*p*CMF C*c* maintains the overall secondary structure and global fold of wild-type (WT) C*c,* as inferred from circular dichroism (CD) (**Figure 1b**) and ^{1}H-^{15}N heteronuclear single-quantum correlation (HSQC) nuclear magnetic resonance (NMR) spectra (**Figure 1c**), respectively. Also, the native heme axial coordination was preserved, as indicated by 1D ^{1}H NMR data (**Figure 1d**). The NMR spectra of reduced Y48*p*CMF C*c* were extensively assigned: triple-resonance experiments (**Table S1**) allowed us to detect and assign 91 backbone amide signals and the sequential connectivities for most residues of the protein. Aliphatic side-chain signals were assigned using 3D HBHA(CO)NH and 3D HCCH-TOCSY experiments, leading to the assignment of most (96.4%) of the side-chain proton resonances. The ^{15}N-H resonance of *p*CMF48 was undetectable because the residue was not ^{15}N-enriched. Four proline residues (Pro30, Pro44, Pro71 and Pro76) interrupt the sequential HN-HN connectivity. Additionally, in contrast to WT C*c*, we could not detect the amide protons of the Thr49, Ala51, Gly56 and Ile57 residues. However, the WT spectra also only had four amide protons that could not be detected (Gly1, Glu21, Thr28 and Gly84) under similar experimental conditions. Further, in contrast to WT C*c*, the signals from Asn31, Gly45 and Ser47 in *p*CMF48 C*c* were significantly weaker than the rest. The largest chemical-shift perturbations for backbone amides induced by the modified residue at position 48 are confined to nearby residues (**Figure S1**).

Assigning ^{1}H resonances to the heme substituents and ^{1}H (and ^{13}C) signals to the aromatic side chains was required for analyzing additional 2D maps (*i.e.* COSY and ^{1}H-^{15}N NOESY) (**Table S1**). Assignment of the Cδ_1, Cδ_2, Cε_1 and Cε_2 aromatic signals from

the *p*CMF48 side-chain required the acquisition of an aromatic ^{1}H-^{13}C HSQC spectrum recorded in a natural abundance of ^{13}C (**Figure 1e**). The assignment of the *p*CMF48 side-chain signals involved the complete assignment of the 2D ^{1}H-^{15}N NOESY.

Numerous residues (Val20–Asn31, Thr40–Trp59 and Ile75–Glu90) displayed signals attributable to a second, minor protein conformation, which had a 1:10 ratio in intensity. Hereafter, only the major form was considered for structure calculations.

We assigned a 96% of all the ^{1}H signals for the major form. Structural information derived from 2D and 3D NOESY maps supported the presence of 5 α-helical regions (labelled α_1 to α_5) with typically strong HN-HN (*i, i*+1), medium-range Hα-HN (*i, i*+3) and Hα-HN (*i*, *i*+4), interresidual NOEs. These regions spanned the sequence stretches Val3–Lys13, Ala50–Asn54, Glu61–Glu69, Pro71–Tyr74 and Lys88–Thr102, resembling those in the NMR structure of reduced WT C*c* (33). In total, we observed and assigned 2,176 meaningful NOEs, corresponding to 20.8 relevant restraints per residue on average (**Figure S2**). The 71 ϕ and 71 ψ dihedral angle constraints were derived from ^{15}N, ^{13}C', ^{13}Cα, ^{13}Cβ and Hα chemical shifts, using TALOS+ (34). The heme moiety was included in the calculations as previously reported for WT cytochromes (35, 36), assuming an intact heme iron coordination as supported by the XAS spectroscopic data (see next section).

Two-hundred structures were calculated by CYANA, and the twenty structures with the lowest target-function (TF) value were selected to form a representative family. The range of TF values was 0.38–0.98 Å^2, highlighting the high accuracy between calculated and experimental distances. Further refinement of the 20 lowest TF structures involved restrained energy minimization and restrained molecular dynamics (RMD) computations. A final restrained energy minimization carried out on the structure with the lowest root-mean square deviation (RMSD) to the average for each of the 20 trajectories. The overall quality of the 20 lowest TF ensemble was good, according to PROCHECK G-factor (37)

MolProbity clash-scores (38) and other structural quality indicators (**Table S2**). Most residues were in the Ramachandran plot favored regions, whereas Cys14, Cys17, His18, Val20, Lys37 and Asn70 were in the generously allowed ones, as also observed for the solution structure of WT C*c* (33, 39). Cys14, Cys17 and His18 are covalently bonded to the heme moiety, thereby straining their backbone conformation, as already described for *c*-type cytochromes (35, 36). As an additional control, we performed 20 ns unrestrained molecular dynamics (MD) simulations of the final minimized conformers without any geometrical restraint. The RMSD for the main-chain atoms was about 1.55 Å at the plateau, hardly drifting (0.122 pm ns^{-1}), as expected for a stable structure (**Figure S3**).

The overall fold of Y48*p*CMF C*c* is very similar to that of the WT species (**Figure S4**), with RMSD values for the backbone nuclei of 1.67 ± 1.01 Å (**Figure 2a,b)**. However, the two structures differ in the mutation-containing loop Ω_{NY} (residues 40–57; **Figure 2b**). This is consistent with the chemical-shift differences (**Figure S1**) and the RMSD between the NMR solution structure of WT C*c* (PDB ID: 1J3S) (33) and the refined lowest-TF Y48*p*CMF C*c* (**Figure S5a**). An increased dynamics in the loop Ω_{NY} has been recently observed in the G41S variant of C*c* (41). The Ω_{NY} loop (also known as foldon V) and helix α_2 constitute the less-stable folding unit of C*c* (42). Unlike Tyr48 in the WT species, the *p*CMF48 residue presents a very low number of ^{1}H-^{1}H NOEs (**Figure S2**) and a high RMSD value within the family (**Figure 2c** and **Figure S5b**). A decrease in the number of detectable NOEs can generally be attributed to either a partial assignment of the residue or an increased internal mobility. In our case, the highly dynamic behavior of the *p*CMF48 residue was confirmed from further analysis of internal motions within the ns-ps time scale (see below).

Other regions of the Y48*p*CMF C*c* structure that differed from that of WT C*c* belong to the 19–36 Ω_G-loop (part of foldon II) and the 71–85 Ω_R-loop (foldon IV) comprising Met80 and helix α_4. The RMSD values for backbone atoms of residues from Val20 to Gly29 of

Y48*p*CMF C*c* are higher (2.75 ± 1.50 Å) than those for the same residues of WT C*c* (**Figure S5a**). In the second loop, the observed differences are mainly restricted to side chains. In fact, the RMSD values for backbone and heavy atoms are 1.18 ± 0.37 Å and 1.77 ± 0.71 Å, respectively. Residues included in the Ω_R loop indeed displayed double conformation, suggesting the presence of conformational equilibria (**Figure S5a**).

The ensemble of structures for Y48*p*CMF C*c* is very precise, except for residues surrounding the mutation. The backbone RMSD to the mean is 0.89 ± 0.01 Å for the whole protein and drops to 0.53 ± 0.12 Å when the mutation surroundings are excluded (residues 40–57) (**Figure S5b**). As expected, the highest RMSD values correspond to the 40–57 Ω_{NY} loop and the nearby residues Val20–Gly29 in loop Ω_G, whose global backbone RMSD values were 1.79 ± 0.53 Å and 0.78 ± 0.23 Å, respectively. These segments also exhibited a larger conformational variability in their secondary structure elements along the MD trajectory (**Figure S3b,c**). High RMSD values along the Val20–Gly29 stretch are typical in C*c* homologs (35, 36). They are also consistent with NMR signals revealing secondary conformations for the His26–Pro30 stretch. Moreover, the nearby Asn31 amide signal is weak, suggesting a high mobility. Notably, all these residues contact the Ω_{NY} loop, comprising the Y48*p*CMF mutation.

Further, the highest RMSD values mapped to the Ω_{NY} loop. Consistently, signals from this region undergo a drastic reduction of their ^{1}H-^{1}H NOE cross-peaks. The intensities of the amide signals of Gly45 and Ser47 in Y48*p*CMF C*c* were severely decreased, while those from Thr49, Ala51, Gly56 and Ile57 were undetectable. The Ω_R loop also contains some residues with high RMSD values (**Figure S5b**). The global RMSD value for backbone atoms of the 71–85 Ω_R loop is equal to 0.76 ± 0.20 Å. Notably, the end of the Ω_R loop shows high RMSD values in WT cytochromes (35, 36).

The heme iron coordination is insensitive to Tyr48 phosphorylation

We tested the effects of the mutation on the heme iron coordination environment and the axial coordination restraints used in our structure computations by using X-ray absorption spectroscopy (XAS), studying both WT and Y48*p*CMF species (**Figure 2d** and **Figure S5c-f**). The absorption spectra of the two proteins are almost identical. The X-ray absorption near-edge structure (XANES) region of the absorption spectra for both proteins are superimposed (**Figure S5c**). The absence of any shift in the energy position of the absorption edge indicates that the mutation did not affect the electron density at the Fe center.

Likewise, the extracted extended X-ray absorption fine structure (EXAFS) signals of the WT and Y48*p*CMF C*c* species were highly similar. However, small differences in high wave vector (*k*) values can be observed (**Figure S5d**), as well as in the slightly lower amplitude of the Y48*p*CMF protein. While the corresponding Fourier transforms are also very similar (**Figure S5e**), the amplitude of the first peak is lower and broader in the Y48*p*CMF C*c* species, suggesting a larger degree of disorder. The dynamic disorder for the two proteins should be similar, as the measurements were performed at cryogenic temperatures in both cases. Hence, the differences in disorder are due to a larger static disorder in Y48*p*CMF C*c*. The main scattering paths contributing to this peak originate from the four nitrogen atoms of the porphyrin ring, although contributions of the nitrogen and sulphur axial ligands have also been included. The fit to the data requires the addition of the paths involving the eight porphyrin carbons closest to the iron atom, beyond the first coordination sphere. In addition, the multiple scattering paths involving these atoms were also included. Fits were performed in R space but also reproduced well the spectra in *q* space (**Figure S5f**). The parameters obtained from the best fit to the data revealed that the distances between the iron atom and its first coordinating ligands are insensitive to the Y48*p*CMF mutation (**Table S3**). Specifically, the distances from the iron center to the axial S ligand are 2.26 ± 0.001 Å and 2.25 ± 0.001 Å in the WT and phosphomimetic mutant species, respectively (**Figure 2d**). Data analyses also

showed that the value for the Debye-Waller factor corresponding to the path involving the four porphyrin nitrogen atoms increased from 0.0012 ± 0.0006 $Å^2$ in the WT species to 0.003 ± 0.001 in the Y48*p*CMF mutant. These data are consistent with the preserved chemical-shift pattern of the iron axial ligands and heme substituents observed in 1D ^1H NMR (**Figure 1d**), which have been reported to be sensitive indicators of the heme iron electronic structures (35, 36). The pattern of the observed NOEs for the heme substituents also supports an overall intact heme pocket, with the exception of the mutation site. Still, the ensemble of structures shows a small change in the orientation of Phe82 with respect to the porphyrin ring (**Figure S6**).

Phosphorylation of Tyr48 enhances internal mobility in cytochrome *c*

NMR relaxation measurements were performed to evaluate the dynamics of WT and Y48*p*CMF C*c*. The Y48*p*CMF substitution slightly affected both relaxation rate (R_1 and R_2) parameters (**Table S4**). The rotational correlation time of the phosphomimetic mutant (6.96 ± 0.02 ns) was higher than that of the WT form (6.33 ± 0.02 ns), in agreement with the small increase (p_{nul} values of approximately 10^{-251}) in the average gyration radius, from 12.95 ± 0.07 Å to 13.04 ± 0.06 Å, as calculated by MD. Indeed, phosphorylation can alter protein dynamics at different timescales and cause conformational rearrangements, such as the formation of secondary conformations (43, 44).

Comparing R_1, R_2 and heteronuclear NOE (HetNOE) relaxation measurements recorded on the two proteins revealed that the Ω_{NY} loop of Y48*p*CMF C*c* exhibits a high mobility in the ps-ns time scale (**Figure 3**). Indeed, the Gly41–Lys55 segment showed a drastic drop of HetNOE values in the mutant species (**Figure 3a**). Further, the amide R_1 rates for the sequence stretch of Tyr46–Lys55 in Y48*p*CMF C*c* differ from those in WT C*c* (**Figure 3b**). In addition, R_2 analyses reveals three regions undergoing conformational exchange in the μs-ms time scale: His26–Thr28, Thr40–Trp59 and Ile75–Thr78 (**Figure 3c**). This behavior agrees with the reduced intensity or lack of detection of the amide

signals belonging to these stretches, as compared to the WT form. Furthermore, some regions within the protein displayed signals corresponding to double conformations in the 2D ^{1}H NOESY spectra—namely, Val20–Asn31, Thr40–Trp59 and Ile75–Glu90, indicating the presence of conformational equilibria between two different structures occurring on a slow-time scale with respect to the NMR chemical shift. This dynamics involves residues located in a defined region surrounding the non-canonical amino acid (**Figure 3d**). Altogether, the NMR relaxation measurements of Y48*p*CMF C*c* agree with the per-residue S^2 order parameter values computed with TENSOR (45) (**Figure 3e**).

Hydrogen-deuterium exchange experiments showed that a common core region is protected from solvent amide-hydrogen exchange in both C*c* species. Nevertheless, a substantial number of amides become unprotected in *p*CMF48 C*c* (**Figure S7**). The newly accessible amide protons in the phosphomimetic mutant (Gly29, Gly37, Arg38, Thr40, Gln42 and Trp59) are located in the surroundings of *p*CMF48 and the nearby Ω_G loop, in agreement with their high mobility in the μs-ms time scale.

Tyr48 phosphorylation modulates the interaction of cytochrome *c* with its mitochondrial partners in the electron transfer chain

C*c* carries electrons from C*bc*$_1$ to C*c*O within the ETC. To elucidate more details about the process, we analyzed the molecular recognition between the soluble N-terminal domain of plant cytochrome c_1 (Cc_1) or bovine C*c*O with the phosphomimetic human Y48*p*CMF C*c.* The human and plant N-terminal domains of Cc_1 have a 62% overall sequence identity and similar charge distributions on their molecular surfaces (46), whereas the bovine and human C*c*O are evolutionarily-related proteins, with 91% and 96% sequence identity and homology, respectively.

Two binding sites for human and plant C*c* on plant Cc_1 have been recently reported (46, 47). The proximal site is located near the heme moiety and is compatible with electron

transfer, while the distal site lies far from the heme group and probably constitutes a local energy minimum of the encounter ensemble.

To test how Tyr48 phosphorylation affects the conformation of the Cc_1-C*c* complex, we recorded ^{1}H-^{15}N HSQC spectra upon titration of ^{15}N-labeled reduced C*c* with unlabeled reduced Cc_1. Several amide signals exhibited significant chemical-shift perturbations (CSPs), thus indicating a fast exchange rate within the NMR time scale (**Figure 4a,b**). Average amide CSPs ($\Delta\delta_{Avg}$) were larger than 0.075 ppm for eleven residues: Gln16, Lys27, Gly29, Ala50, Lys55, Ile58, Lys72, Gly77, Met80, Ile81 and Val83 (**Figure 4b**). The fits of CSPs along the titration suggested that Cc_1 binds two Y48*p*CMF C*c* molecules, as previously found with the WT C*c* species (46, 47) (**Figure 4c**). Using NMR spectroscopy, the dissociation constant (K_D) values for the Cc_1-Y48*p*CMF C*c* complex were estimated to be 0.6 μM and 102 μM for the proximal and distal binding sites, respectively. All the perturbed residues, except Lys55 and Ile58, surround the heme crevice, as previously described for the interaction between WT C*c* and Cc_1 (46, 47) (**Figure 4d**). In fact, this region constitutes a very well-conserved interaction surface in *c*-type cytochromes (48-51). Lys55 and Ile58, in turn, are located in the Ω_{NY} loop, which undergoes a conformational exchange in free Y48*p*CMF C*c* (**Figure 4d**). In addition, significant CSPs ($\Delta\delta_{Avg} \geq 0.05$ ppm) were detected for Lys7, Lys13, His26, Lys39, Ala43, Thr78, Lys86, Lys88 and Glu89. Interestingly, Lys8, Lys13, Lys27, Lys72 and Lys86 also experienced large CSPs, as previously reported for the interaction between WT C*c* and Cc_1 (46, 47).

To obtain further data on the binding affinity and stoichiometry of the interaction between the two redox proteins, isothermal titration calorimetry (ITC) experiments were performed on both redox states. The isotherms obtained by titrating reduced Y48*p*CMF C*c* with reduced Cc_1 are displayed (**Figure 4e**, *left* panel). For the interaction between C*c* and Cc_1, the isotherm clearly shows two components with opposite signs in their respective enthalpy terms, thereby indicating the presence of two binding sites, in agreement with

316 the NMR data herein presented and previous reports on the WT species (46, 47). Indeed,
317 all data fit a model with two independent binding sites in the corresponding C*c* partner
318 (**Table S5**). The interaction between Y48*p*CMF C*c* and Cc_1 was entropy-driven. At pH
319 7.4, K_D value at the proximal site was half that observed for WT C*c*, whereas that at the
320 distal site was four times higher (**Table S5**). This could be ascribed to the extra negative
321 charge at position 48, which alters the surface electrostatic potential of the hemeprotein
322 (**Figure S8**). Both Cc_1–Y48*p*CMF C*c* and Cc_1-C*c* complexes in their oxidized states
323 showed similar thermodynamic and equilibrium parameters at both acidic and basic pH
324 values. The only exception was the K_D value for the oxidized Cc_1–Y48*p*CMF C*c* complex,
325 at the proximal site of Cc_1, that was approximately four times lower than that for the
326 oxidized Cc_1-WT C*c* adduct at pH 8.5. ITC measurements of the oxidized Cc_1–Y48*p*CMF
327 C*c* complex were not run at pH 7.4 because the pK_a for the alkaline transition, which is
328 specific to the ferric state (52), shifts to neutral pH upon Tyr48 phosphorylation (31).
329 Hence, the WT and phosphomimic forms of oxidized C*c* can differ in their sixth axial
330 ligand at pH 7.4 (**Table S5**).

331 In addition, we analyzed the binding affinity of the cross-complex between the reduced
332 species of bovine C*c*O and human Y48*p*CMF C*c* by ITC. The isotherm inflexion point
333 lies at a 2:1 Y48*p*CMF-C*c*:C*c*O ratio, thereby indicating the presence of two binding sites
334 on C*c*O, as previously found for WT C*c* (46, 53, 54). The best fit was achieved when the
335 model used distinct K_D values for the two independent binding sites (**Figure S9**). The
336 resulting isotherms likewise fit to such model yielding different μM-ranging K_D values
337 (**Figure 4e,** *right* panel, and **Table S6**) and enthalpy-driven interactions. Both the C*c*O
338 *proximal* and *distal* sites had lower affinities for Y48*p*CMF C*c* than the WT species, as
339 previously reported (46) (**Table S6**). Altogether, these data agree with previous steady
340 state kinetic analysis that demonstrated a binding model with more than one molecule of
341 C*c* per molecule of C*bc*$_1$ (55) and with kinetic-based models that proposed the existence
342 of alternative, non-productive binding sites for horse C*c* in bovine C*c*O (54). In addition,

direct binding studies performed by gel filtration between several mammalian C*c* and bovine C*c*O evidenced a 2:1 stoichiometry, in which C*c* bound to a first site with a dissociation constant within the nM range and to a second site with less affinity (53).

To assess the functional ability of Y48*p*CMF C*c* to reduce respiratory complex IV, we tested the C*c*O activity of isolated complex IV or C*c*-free mitochondria (ΔC*c*) from yeast cells grown with glucose as a carbon source (**Figures 5a and S10a**). In both cases, the C*c* oxidation rate was at least two-fold higher with Y48*p*CMF C*c* than with WT C*c*, thereby suggesting that Tyr48 phosphorylation enhances the ability of C*c* to donate electrons to complex IV. Direct measurements of O_2 consumption were consistent with such data (**Figure S10b**). Interestingly, the C*c*O activity was positively regulated by the human membrane proteins hypoxia-inducible domain family members 1A and 2A (HIGD1A and HIGD2A), which promote cell survival under hypoxia. HIGD2A was successfully expressed in cell-free expression systems combined with n-dodecyl-β-D-maltoside, as previously reported for HIGD1A (56) (**Figure S11a-c**). HIGD1A significantly increased the rate of C*c*O-catalyzed oxidation of Y48*p*CMF C*c* (**Figure 5b**), as reported for WT C*c* (57). Strikingly, HIGD2A induced an even a stronger positive effect than HIGD1A (**Figure 5b**). Nevertheless, the HIGD-dependent increase in C*c*O activity was slightly lower with Y48*p*CMF C*c* (**Figure 5b**). This may be due to HIGD-dependent changes in either the complex IV affinity towards C*c* or in the restraints of C*c* diffusion (channeling) from Cc_1 to complex IV. A direct C*c*-HIGD interaction can also not be excluded.

To confirm the HIGD-mediated regulation of the C*c*O activity in a cellular context, we isolated mitochondria from different yeast strains grown either with glucose (YPD medium), which supports fermentation and respiration, or with the non-fermentable carbon sources lactate and galactose (YP-Gal) (58). Under both metabolic conditions, the isoformic respiratory supercomplex factors 1 (Rcf1, formerly Aim31) and 2 (Rcf2, formerly Aim38) are constitutively expressed (**Figure 5c**, *inset*), in agreement with their

role in C*c*O activity and supercomplex stability (58-60). Rcf1 is a yeast orthologue of the human HIGD1A and HIGD2A proteins, whereas Rcf2 is specific to yeast. The external membranes of isolated mitochondria were then permeabilized to allow the entry of exogenous WT or Y48*p*CMF C*c*. Under these conditions, mitochondria isolated from a yeast strain deficient of both Rcf1 and Rcf2 (ΔRcf1/2), as verified by western blot, displayed an endogenous C*c*O activity lower than those isolated from WT yeast (WT_{Rcf}), no matter which type of exogenous hemeprotein—WT or Y48*p*CMF C*c*—was used for supplementing (**Figure 5c**). This indicates that Rcf1 and Rcf2 act as positive modulators of C*c*O activity, similar to human HIGD proteins. In mitochondria isolated from yeast grown with non-fermentable carbon sources, the Rcf-mediated increase in C*c*O activity was less prominent when Y48*p*CMF C*c* rather than WT C*c* was added as an exogenous electron donor, in agreement with the *in vitro* behavior of isolated proteins (**Figure 5b**). This suggests that Tyr48 phosphorylation makes C*c* less sensitive to the enhancer mechanism of the Rcf proteins and/or to the ability of Rcfs to stabilize the Cbc_1-C*c*O supercomplexes (**Figure 5c)**. In fact, Rcf1 and Rcf2 promote the supercomplex assembly, preferably in mitochondria from yeasts grown in a respiratory-based medium (**Figure 5d** and **Figure S11d**). This is especially remarkable when comparing the band intensities in an anti–COX-2 immunoblot (**Figure 5d**). Note that such OxPhos supercomplexes could show a certain degree of heterogeneity in their composition, since the gene transcription of COX5a and COX5b—which encode for two C*c*O isoforms—are repressed and active, respectively, in the aerobic-to-anaerobic metabolic transition (61). Moreover, the faint band pattern of ΔRcf1/2 strains grown in YPD medium in the BN-PAGE corresponds to supercomplexes, thus suggesting that other factors may contribute to their assembly (**Figure 5d** and **Figure S11d**).

Altogether, our data suggest that phosphorylation of C*c* at Tyr48 modulates the mitochondrial ETC (**Figure 5e**). Such a posttranslational modification allows a fast adaptation of the hemeprotein function to changing cell conditions. The population of

C*bc*$_1$-C*c*O supercomplexes is less prominent in the presence than in the absence of glucose, although Rcf proteins are still expressed. In any case, C*c* channeling from C*bc*$_1$ towards C*c*O is impaired. At a physiological pH, Tyr48 phosphorylation thus favors binding of C*c* to the proximal rather than to the distal site of C*c*$_1$. Under respiration-based growth, the Rcf proteins preferably associate directly with the OxPhos supercomplex, bridging C*bc*$_1$ and C*c*O. However, the weaker Y48*p*CMF C*c*-C*c*O binding, along with the loss of the distal site on C*c*$_1$ due to phosphorylated C*c*, impairs the channeling of C*c* molecules that functionally connects C*bc*$_1$ with C*c*O, which has been proposed to occur with WT C*c* (46, 47). As a consequence, Y48*p*CMF C*c* is less efficient than WT C*c* as an electron carrier towards C*c*O in the context of OxPhos supercomplexes.

Tyr48-phosphorylated cytochrome *c* acts as an improved peroxidase-like enzyme, in particular when bound to cardiolipin-containing liposomes

Assembly of the mitochondrial protein membrane complexes C*bc*$_1$ and C*c*O into OxPhos supercomplexes enables more efficient electron flow and decreases ROS levels generated by the ETC (62). The phospholipid CL, located in the inner mitochondrial membrane, also stabilizes the resulting supercomplexes (63) in a HIGD/Rcf-independent manner (58). In addition, CL interacts with C*c* in a two-step binding reaction (64): in the first step, the so-called A-site at the C*c* surface makes transient electrostatic contacts with the membrane; in the second step, hydrophobic forces drive the formation of a tight and stable C*c*-CL complex, with one of the CL acyl chains entering the hydrophobic groove of C*c* (termed the C-site) (65-67). C-site binding then triggers C*c*-regulated CL peroxidation under oxidative stress and induces early apoptosis (39). Interestingly, several residues of C*c* (Lys22, Lys27 and His33) become protonated at low pH to form an extra binding site – the so-called L-site – that facilitates the electrostatic interaction of C*c* with mitochondrial membranes (68).

Within this frame, we analyzed how tyrosine phosphorylation can fine-tune the affinity of C*c* towards CL-containing liposomes, analyzing binding of C*c* species to liposomes in HEPES buffer at a physiological pH value by electrophoretic mobility shift assays (EMSA) in native agarose gels (**Figure 6a,b**). To compare the binding properties of C*c* species to the CL-containing liposomes of 4:1 DOPC:TOCL (1,2-dioleoyl-*sn*-glycero-3-phosphocholine:1,1'2,2'-tetraoleoylcardiolipin) or to the liposome DOPC alone, we measured the mobility profiles of C*c* at different C*c*:lipid ratios. While both WT and Y48*p*CMF C*c* bound to DOPC:TOCL and DOPC vesicles, their binding affinity for the CL-free DOPC liposomes seemed to be lower (**Figure 6a,b**). Notably, the presence of free hemeprotein at high lipid concentrations suggested that Y48*p*CMF C*c* has a lower affinity than WT towards DOPC:TOCL liposomes (**Figure 6b**), as recently observed for the phosphomimetic mutant S47D C*c* (69). Another interesting finding is the unspecific interaction of C*c* —either the WT or Y48*p*CMF species—with DOPC vesicles (**Figure 6a,b**).

ITC measurements corroborated these EMSA data. ITC experiments were performed under aerobiosis to mimic physiological conditions, despite using degassed samples. This may result in partial oxidation of C*c* upon binding to liposomes, as previously reported (70). ITC analysis yielded the apparent K_D values for the first binding event of 427 μM (WT C*c*) and 780 μM (Y48*p*CMF C*c*) (**Figure 6c**). Data for the interaction of WT C*c* with liposomes are consistent with the K_D values reported before (67, 71, 72, 73), but they diverge from the lower K_D values reported in the literature (74) and the A/C two-site binding model described by Kinnunen and co-workers (65, 66). Such discrepancies are still unresolved and further research is necessary to harmonize data from all these different binding assays in a unified and single model. The interaction with CL resulted in apparent ΔH values equal to 2.75 kcal mol^{-1} for WT C*c* and 38.97 kcal mol^{-1} for Y48*p*CMF C*c*. The differences in K_D indicate a small change in binding energies (of approximately 6 kcal mol^{-1}). Hence, the changes in ΔH are indicative of enthalpy-entropy

compensation effects, which are compatible with the electrostatic change resulting from the extra carboxylate group of the Y48*p*CMF species. Further, an exothermic process can be observed, with longer peak equilibrium times upon successive lipid additions. In this case, the apparent Δ*H* values with the WT and Y48*p*CMF C*c* species were equal to –6.97 kcal mol^{-1} and –47.84 kcal mol^{-1}, respectively, but the apparent K_D value (of approximately 1 mM) was practically the same with the two C*c* species. Altogether, our EMSA and ITC assays indicate that Y48*p*CMF C*c* binds to CL-containing liposomes with a slightly lower affinity than WT C*c*.

WT C*c* undergoes CL-dependent conformational changes that allow H_2O_2 to access the heme crevice (73). Hence, we addressed whether the affinity differences between WT and Y48*p*CMF C*c* for CL could affect their peroxidase activity. In the absence of CL-containing liposomes, Y48*p*CMF C*c* exhibited a three-fold higher peroxidase activity than WT C*c* (**Figure 6d**). However, the presence of TOCL/DOPC vesicles, at a 1:100 C*c*:lipid ratio, increased the enzymatic activity of both WT and Y48*p*CMF C*c*, similar to that observed for other phosphomimetic C*c* mutants (69). Note that the slightly lower peroxidase activity increment observed for Y48*p*CMF C*c* is likely due to its higher population of free protein as compared to WT C*c* (**Figure 6b,d**).

Tyr48 phosphorylation is an anti-apoptotic posttranslational modification

Phosphorylated C*c* may be more easily released from mitochondria because of its lower affinity towards CL, as inferred from EMSA and ITC assays. Translocation to the cytosol could thus enable phosphorylated C*c* to interact with Apaf-1 and to assemble the caspase-activating apoptosome. However, cytosolic caspase-3 activation was decreased by about 60% in the presence of the Y48*p*CMF C*c* mutant (**Figure 6e**). This is in agreement with the behavior previously reported for the Y48E C*c* mutant, which exhibits a lower ability than WT C*c* to activate not only caspase-3 (26) but also

procaspase-9 by non-functional apoptosome assembly (27). These results could thus be indicative of an anti-apoptotic function of C*c* when phosphorylated at position 48.

DISCUSSION

Here we tackle the structural and functional characterization of the Y48*p*CMF variant of human C*c.* This mutation mimics protein phosphorylation at Tyr48 by adding a negative charge and slightly increasing the side-chain size while keeping the aromatic ring. A recent spectroscopic analysis of Y48*p*CMF C*c* showed a singular shift of the typical alkaline transition pK_a to physiological pH values (31), as is the case with the Y48E C*c* mutant (26, 27). Here, we report NMR-based structure computations that indicate that Tyr48 phosphorylation maintains the core foldon of C*c* but increases internal motions in the loops Ω_{NY}, Ω_R and Ω_G. Specifically, the Ω_{NY} loop, the most unstable folding unit of the hemeprotein, becomes looser and reaches conformational equilibria in Y48*p*CMF C*c*. Enhanced motions at the Ω_G and Ω_R loops could be associated to the shift in the alkaline transition pK_a. Indeed, these two loops hold the residues that provide the iron axial ligands, which are observed to at least partially lose their metal coordination in the alkaline form (75). This is in contrast to XAS data that suggest that axial coordination remains untouched. However, the cryogenic temperatures at which the XAS spectra were recorded may amplify the most stable structures and reduce contributions from minority species with a high disorder, which are undetectable.

The local but substantial changes in conformation and dynamics of the regions surrounding the Y48*p*CMF mutation increased the solvent accessibility of the porphyrin ring, thereby enhancing cytochrome peroxidase activity. Thus, Y48*p*CMF C*c* proficiently scavenges ROS and avoids damage of cellular components (**Figure 7**). Our findings also indicate that Y48*p*CMF C*c* binds to mitochondrial CL with a lower affinity than WT C*c* but Y48*p*CMF C*c* shows a higher peroxidase activity upon binding to liposomes.

503 According to the literature, both events may facilitate C*c* translocation to the cytoplasm
504 during apoptosis (76). However, phosphorylation at Tyr48 hinders the proapoptotic
505 activity of extramitochondrial C*c*, similar to the function of HIGD1A protein in ischemia
506 and tumorigenesis (77). Indeed, both HIGD1A and Y48*p*CMF C*c* act as pro-survival
507 proteins by preventing apoptotic caspase activation (**Figure 7**) (78).

508 As expected, the Y48*p*CMF mutation affects the binding mode of C*c* to its well-known
509 respiratory partners C*bc*$_1$ and C*c*O. Not surprisingly, the enhanced internal motions of
510 the loops Ω_{NY} and Ω_R and the electrostatic change at the interaction patch resulting from
511 the additional carboxyl group affect the interaction of Y48*p*CMF C*c* with the two
512 membrane complexes. The mutation-induced changes in electrostatics and in solvation
513 at the interface also concur for the interaction of reduced Y48*p*CMF C*c* with the distal
514 sites of C*c*O (and C*c*$_1$), as inferred from the high decrease in the dissociation enthalpies
515 and the strong (or moderate) enthalpy-entropy compensation herein reported. Indeed,
516 the binding of Y48*p*CMF C*c* on the C*c*$_1$ surface is weak and functionally irrelevant at the
517 distal site but is favored at the proximal site (**Figure 5e**). When the turnover of the redox
518 carrier at the main site is considered, the high affinity of reduced Y48*p*CMF C*c* inhibits
519 its own replacement by oxidized C*c* molecules, thereby impairing the electron transport.

520 The C*c*:C*c*O complex keeps its interface solvated, according to the recent X-ray
521 diffraction structure (79), which displays a protruding lysine sidechain in C*c*O pointing to
522 Tyr48 in C*c*. A salt bridge involving phosphorylated Tyr48 would restrain the Ω_{NY} loop.
523 The increase in the dissociation constant (K_D) of the complex between Y48*p*CMF C*c* and
524 C*c*O (this work) and the decrease in the Michaelis constant (K_M) of phosphorylated C*c*
525 with C*c*O (80) indicate that K_M is mainly governed by the catalytic step. This agrees with
526 the larger C*c*O-driven oxidation rate of Y48*p*CMF C*c* compared with that of WT C*c* at the
527 limiting protein concentrations in the enzymatic activity assays used here. In this context,
528 the ca. 60 mV decrease in the E_0 of Y48*p*CMF C*c* (31) may facilitate the electron flow
529 from C*c* to C*c*O although it may impair C*c* reduction by C*bc*$_1$. In other words, Y48*p*CMF

530 C*c* exhibits a reduced ability as oxidizing agent (it is less capable than WT C*c* to receive
531 electrons from Cc_1), but displays an increased capacity as reducing agent (it is a better
532 electron donor to C*c*O than WT C*c*). It is well known that the catalytic step can be tuned
533 by conformational changes of C*c* upon binding to C*c*O (51). Strikingly, these changes
534 resemble the prominent internal dynamics of Y48*p*CMF C*c*, which could also explain not
535 only the change in E_0, but also the shift in the alkaline transition pK_a of oxidized Y48*p*CMF
536 C*c* (31). Therefore, the transition from reduced to oxidized Y48*p*CMF C*c*, which is
537 accompanied by a change in the iron axial ligand at physiological pH, is expected to have
538 a high-energy barrier (81). Hence, such conformational changes might be the limiting
539 step for Y48*p*CMF C*c* oxidation inside the complex.

540 Under nutrient and oxygen depletion, a dysfunctional mitochondrial ETC and OxPhos
541 can lead to many human diseases, including pathologies like ischemia and cancer (24).
542 The nexus in both disorders could be the control of mitochondrial ET rate by C*c*
543 phosphorylation (23), which has indeed been reported to efficiently fine-tune respiratory
544 rates (80). Even though HIGD-mediated assembly of C*bc*$_1$ and C*c*O into OxPhos
545 supercomplexes preferably occurs under low glucose conditions, the decrease in both
546 the C*c*O activity and the binding affinity towards Cc_1 and C*c*O resulting from the
547 enhanced dynamics of Y48*p*CMF C*c* could explain the disruption of C*c* channeling inside
548 the C*bc*$_1$-C*c*O supercomplex, thus slowing down the ETC flow (**Figure 7**).

549 Intriguingly, not only respiratory supercomplex formation (59, 60)–whose structure has
550 been recently solved (82, 83)–but also C*c* phosphorylation, and the resulting decrease
551 in the ETC rate, could help to keep ROS levels low and to guarantee cell survival.

552 Tyr48-phosphorylated C*c* could be targeted as a biomarker of mitochondrial dysfunction
553 with associated pathological states, such as ischemia/reperfusion and cancer.
554 Deciphering the details of the phosphorylated C*c*–controlled complex network requires
555 accurate structural and dynamic analyses, to eventually develop robust therapeutic

approaches to foster or silence—as required—the pro-survival action of phosphorylated C*c* reported here.

MATERIAL AND METHODS

Methods and any associated references are available in the Supplementary Information.

Accession codes. NMR assignments and PDB coordinates for the Y48*p*CMF C*c* were deposited in the Biological Magnetic Resonance Data Bank (BMRB; entry 25660) and PDB (2N3Y code) databases.

All biological samples were obtained from bacteria, yeasts or human cell extracts, in fully compliance with the University of Seville Ethical Committee bylaws.

ACKNOWLEDGMENTS

Financial support was provided by the Spanish Ministry of Economy and Competitiveness (Grants BFU2015-71017-P/BMC and BFU2015-19451/BMC, co-founded by FEDER EU), European Union (Bio-NMR-00130 and CALIPSO-312284), Ramon Areces Foundation and Andalusian Government (BIO198). BMB was awarded with a PhD fellowship from the Spanish Ministry of Education (AP2009-4092), and with a short-term travelling fellowship from the European Bio-NMR Project. AGC was awarded a PhD fellowship from CSIC (JaePre-2011-01248). Experimental work was performed in part at the Grenoble INSTRUCT center (ISBG, UMS 3518 CNRS-CEA-UJF-EMBL), with support from FRISBI (ANR-10-INSB-05-02) and GRAL (ANR-10-LABX-49-01) within the Grenoble Partnership for Structural Biology (PSB). We also thank Diamond Light Source for access to beamline I20-scanning (proposal number SP-6011). We acknowledge the NMR services at the Centro di Ricerca di Risonanze Magnetiche (CERM, Florence), the Centro de Investigación, Tecnología e Investigación (CITIUS, Seville) and the Biointeractomics Platform (BIP-cicCartuja, Seville), as well as TA Instruments.

COMPETING INTERESTS

The authors declare no competing interests.

REFERENCES

1. Papa S (1982) Molecular mechanism of proton translocation by the cytochrome system and the ATPase of mitochondria. Role of proteins. *J Bioenerg Biomembr* 14: 69-86.
2. Turrens JF (2003) Mitochondrial formation of reactive oxygen species. *J Physiol* 552: 335-344.
3. Lenaz G, Genova ML (2010) Structure and organization of mitochondrial respiratory complexes: a new understanding of an old subject. *Antioxid Redox Signal* 12: 961-1008.
4. Ray PD, Huang BW, Tsuji Y (2012) Reactive oxygen species (ROS) homeostasis and redox regulation in cellular signaling. *Cell Signal* 24: 981-990.
5. Hou T, Wang X, Ma Q, Cheng H (2014) Mitochondrial flashes: new insights into mitochondrial ROS signalling and beyond. *J Physiol* 592: 3703-3713.
6. Solaini G, Baracca A, Lenaz G, Sgarbi G (2010) Hypoxia and mitochondrial oxidative metabolism. *Biochim Biophys Acta – Bioenerg* 1797: 1171-1177.
7. Lenaz G, Baracca A, Barbero G, Bergamini C, Dalmonte ME, *et al.* (2010) Mitochondrial respiratory chain super-complex I-III in physiology and pathology. *Biochim Biophys Acta – Bioenerg* 1797: 633-640.
8. Corcoran A, Cotter, TG (2013) Redox regulation of protein kinases. *FEBS J* 280: 1944-1965.
9. Helling S, *et al.* (2012) Multiple phosphorylations of cytochrome *c* oxidase and their functions. *Proteomics* 12: 950-959.

612 10. Díaz-Moreno I, García-Heredia JM, Díaz-Quintana A, De la Rosa MA (2011)
613 Cytochrome *c* signalosome in mitochondria. *Eur Biophys J* 40: 1301-1315.
614 11. Wegerich F, Turano P, Allegrozzi M, Möhwald H, Lisdat F (2009) Cytochrome *c*
615 mutants for superoxide biosensors. *Anal Chem* 81: 2976-2984.
616 12. Florence TM (1985) The degradation of cytochrome *c* by hydrogen peroxide. *J Inorg*
617 *Biochem* 23: 131-141.
618 13. Radi R, Thomson L, Rubbo H, Prodanov E (1991) Cytochrome *c*-catalyzed oxidation
619 of organic molecules by hydrogen peroxide. *Arch Biochem Biophys* 288: 112-117.
620 14. Radi R, Turrens JF, Freeman BA (1991) Cytochrome c-catalyzed membrane lipid
621 peroxidation by hydrogen peroxide. *Arch Biochem Biophys* 288: 118-125.
622 15. Martinou JC, Desagher S, Antonsson B (2000) Cytochrome *c* release from
623 mitochondria: all or nothing. *Nat Cell Biol* **2**: E41-43.
624 16. Basova LV, *et al.* (2007) Cardiolipin switch in mitochondria: shutting off the reduction
625 of cytochrome *c* and turning on the peroxidase activity. *Biochemistry* 46: 3423-3434.
626 17. Kagan VE, *et al.* (2009) Cytochrome *c*/cardiolipin relations in mitochondria: a kiss of
627 death. *Free Radic Biol Med* 46: 1439-1453.
628 18. Bertini I, Chevance S, Del Conte R, Lalli D, Turano, P (2011) The anti-apoptotic Bcl-
629 x(L) protein, a new piece in the puzzle of cytochrome *c* interactome. *PLoS One* 6:
630 e18329.
631 19. Martínez-Fábregas J, *et al.* (2013) New *Arabidopsis thaliana* cytochrome *c* partners:
632 a look into the elusive role of cytochrome *c* in programmed cell death in plants. *Mol*
633 *Cell Proteomics* 12: 3666-3676.
634 20. Martínez-Fábregas J, *et al.* (2014) Structural and functional analysis of novel human
635 cytochrome *c* targets in apoptosis. *Mol Cell Proteomics* 13: 1439-1456.
636 21. González-Arzola K, *et al.* (2015) Structural basis for inhibition of the histone
637 chaperone activity of SET/TAF-Iβ by cytochrome *c*. *Proc Natl Acad Sci USA* 112:
638 9908-9913.

639 22. Martínez-Fábregas J, Díaz-Moreno I, González-Arzola K, Díaz-Quintana A, De la
640 Rosa MA (2014) A common signalosome for programmed cell death in humans and
641 plants. *Cell Death Dis* 5: e1314.
642 23. Hüttemann M, *et al.* (2008) Regulation of oxidative phosphorylation, the
643 mitochondrial membrane potential, and their role in human disease. *J Bioenerg*
644 *Biomemb* 40: 445-456.
645 24. Hüttemann M, Lee I, Grossman LI, Doan JW, Sanderson TH (2012) Phosphorylation
646 of mammalian cytochrome *c* and cytochrome *c* oxidase in the regulation of cell
647 destiny: respiration, apoptosis, and human disease. *Adv Exp Med Biol* 748: 237-
648 264.
649 25. Kadenbach B (1968) Incorporation of ^{32}P-phosphate into phosphatides of rat liver
650 mitochondria *in vivo* and *in vitro*. *FEBS Lett* 2: 118-120.
651 26. Pecina P, *et al.* (2010) Phosphomimetic substitution of cytochrome *c* tyrosine 48
652 decreases respiration and binding to cardiolipin and abolishes ability to trigger
653 downstream caspase activation. *Biochemistry* 49: 6705-6714.
654 27. García-Heredia JM, *et al.* (2011) Tyrosine phosphorylation turns alkaline transition
655 into a biologically relevant process and makes human cytochrome *c* behave as an
656 anti-apoptotic switch. *J Biol Inorg Chem* 16: 1155-1168.
657 28. Díaz-Moreno I, García-Heredia JM, Díaz-Quintana A, Teixeira M, De la Rosa MA
658 (2011) Nitration of tyrosines 46 and 48 induces the specific degradation of
659 cytochrome *c* upon change of the heme iron state to high-spin. *Biochim Biophys*
660 *Acta – Bioenerg* 1807: 1616-1623.
661 29. García-Heredia JM, *et al.* (2012) Specific nitration of tyrosines 46 and 48 makes
662 cytochrome *c* assemble a non-functional apoptosome. *FEBS Lett* 586: 154-158.
663 30. Ly HK, Utesch T, Díaz-Moreno I, García-Heredia JM, De La Rosa MA, *et al.* (2012)
664 Perturbation of the redox site structure of cytochrome *c* variants upon tyrosine
665 nitration. *J Phys Chem B* 116: 5694-5702.

31. Guerra-Castellano A, *et al.* (2015) Mimicking tyrosine phosphorylation in human cytochrome *c* by the evolved tRNA synthetase technique. *Chem Eur J* 21: 15004-15012.
32. Ripple MO, Abajian M, Springett R (2010) Cytochrome *c* is rapidly reduced in the cytosol after mitochondria outer membrane permeabilization. *Apoptosis* 15: 563-573.
33. Jeng WY, Chen CY, Chang HC, Chuang WJ (2002) Expression and characterization of recombinant human cytochrome *c* in *E. coli*. *J Bioenerg Biomembr* 34: 423-431.
34. Cornilescu G, Delaglio F, Bax A (1999) Protein backbone angle restraints from searching a database for chemical shift and sequence homology. *J Biomol NMR* 13: 289-302.
35. Baistrocchi P, Banci L, Bertini I, Turano P (1996) Three-dimensional solution structure of *Saccharomyces cerevisiae* reduced iso-1-cytochrome *c*. *Biochemistry* 35: 13788-13796.
36. Banci L, Bertini I, Huber JG, Spyroulias GA, Turano P (1999) Solution structure of reduced horse heart cytochrome *c*. *J Biol Inorg Chem* 4, 21-31.
37. Laskowski RA, Rullmannn JA, MacArthur MW, Kaptein R, Thornton JM (1996) AQUA and PROCHECK-NMR: programs for checking the quality of protein structures solved by NMR. *J Biomol NMR* 8: 477-486.
38. Word JM, *et al.* (1999) Visualizing and quantifying molecular goodness-of-fit: small-probe contact dots with explicit hydrogen atoms. *J Mol Biol* 285: 1711-1733.
39. Rajagopal BS, *et al.* (2013) The hydrogen-peroxide-induced radical behaviour in human cytochrome *c*-phospholipid complexes: implications for the enhanced pro-apoptotic activity of the G41S mutant. *Biochem J* 456: 441-452.
40. Pettersen EF, *et al.* (2004) UCSF Chimera - A visualization system for exploratory research and analysis. *J Comput Chem* 25: 1605-1612.

41. Karsisiotis AI, *et al.* (2016) Increased dynamics in the 40-57 Ω-loop of the G41S variant of human cytochrome *c* promote its pro-apoptotic conformation. *Sci Rep* 6: 30447.
42. Maity H, Maity M, Englander SW (2004) How cytochrome *c* folds, and why: submolecular foldon units and their stepwise sequential stabilization. *J Mol Biol* 34: 223-233.
43. Xiao Y, *et al.* (2014) Phosphorylation releases constrains to domain motion in ERK2. *Proc Natl Acad Sci USA* 111: 2506-2511.
44. Wauer T, *et al.* (2015) Ubiquitin Ser65 phosphorylation affects ubiquitin structure, chain assembly and hydrolysis. *EMBO J* 34, 307-325.
45. Dosset P, Hus JC, Blackledge M, Marion D (2000) Efficient analysis of macromolecular rotational diffusion from heteronuclear relaxation data. *J Biomol NMR* 16: 23-28.
46. Moreno-Beltrán B, *et al.* (2015) Respiratory complexes III and IV can each bind two molecules of cytochrome *c* at low ionic strength. *FEBS Lett* 589: 476-483.
47. Moreno-Beltrán B, *et al.* (2014) Cytochrome c_1 exhibits two binding sites for cytochrome *c* in plants. *Biochim Biophys Acta – Bioenerg* 1837: 1717-1729.
48. Díaz-Moreno I, *et al.* (2005) NMR analysis of the transient complex between membrane photosystem I and soluble cytochrome c_6. *J Biol Chem* 280: 7925-7931.
49. Díaz-Moreno I, Díaz-Quintana A, Ubbink M, De la Rosa MA (2005) An NMR-based docking model for the physiological transient complex between cytochrome *f* and cytochrome c_6. *FEBS Lett* 579: 2891-2896.
50. Volkov AN, Worrall JA, Holtzmann E, Ubbink M (2006) Solution structure and dynamics of the complex between cytochrome *c* and cytochrome *c* peroxidase determined by paramagnetic NMR. *Proc Natl Acad Sci USA* 103: 18945-18950.
51. Sakamoto K, *et al.* (2011) NMR basis for interprotein electron transfer gating between cytochrome *c* and cytochrome *c* oxidase. *Proc Natl Acad Sci USA* 108: 12271-12276.

720 52. Boffi F, *et al.* (2001) pH-dependent local structure of ferricytochrome *c* studied by X-
721 Ray Absorption Spectroscopy *Biophys J* 80: 1473-1479.
722 53. Osheroff N, *et al.* (1983) The reaction of primate cytochromes *c* with cytochrome *c*
723 oxidase. Analysis of the polarographic assay. *J Biol Chem* 258: 5731-5738.
724 54. Garber EA, Margoliash E (1990) Interaction of cytochrome *c* with cytochrome *c*
725 oxidase: an understanding of the high- to low-affinity transition. *Biochim Biophys*
726 *Acta – Bioenerg* 1015: 279-287.
727 55. Speck SH, Margoliash E (1984) Characterization of the interaction of cytochrome *c*
728 and mitochondrial ubiquinol-cytochrome *c* reductase. *J Biol Chem* 259: 1064-1072.
729 56. Klammt C, *et al.* (2012) Facile backbone structure determination of human
730 membrane proteins by NMR spectroscopy. *Nat Methods* 9: 834-839.
731 57. Hayashi T, *et al.* (2015) Higd1a is a positive regulator of cytochrome *c* oxidase. *Proc*
732 *Natl Acad Sci USA* 112: 1553-1558.
733 58. Strogolova V, Furness A, Robb-McGrath M, Garlich J, Stuart RA (2012) Rcf1 and
734 Rcf2, members of the hypoxia-induced gene 1 protein family, are critical
735 components of the mitochondrial cytochrome bc_1-cytochrome *c* oxidase
736 supercomplex. *Mol Cell Biol* 32: 1363-1373.
737 59. Chen YC, *et al.* (2012) Identification of a protein mediating respiratory supercomplex
738 stability. *Cell Metab* 15: 348-360.
739 60. Vukotic M, *et al.* (2012) Rcf1 mediates cytochrome oxidase assembly and
740 respirasome formation, revealing heterogeneity of the enzyme complex. *Cell Metab*
741 15: 336-347.
742 61. Fukuda R, *et al.* (2007) HIF-1 regulates cytochrome oxidase subunits to optimize
743 efficiency of respiration in hypoxic cells. *Cell* 129: 111-122.
744 62. Louro RO, Díaz-Moreno I (2015) Redox Proteins in Supercomplexes and
745 Signalosomes. CRC Press, Taylor, Francis Group, Oxfordshire, UK.

746 63. Zhang M, Mileykovskaya E, Dowhan W (2002) Gluing the respiratory chain together.
747 Cardiolipin is required for supercomplex formation in the inner mitochondrial
748 membrane. *J. Biol. Chem* 277: 43553-43556.
749 64. Belikova NA, *et al.* (2006) Peroxidase activity and structural transitions of
750 cytochrome *c* bound to cardiolipin-containing membranes. *Biochemistry* 45: 4998-
751 5009.
752 65. Rytömaa M, Mustonen P, Kinnunen PK (1992) Reversible, nonionic, and pH-
753 dependent association of cytochrome *c* with cardiolipin-phosphatidylcholine
754 liposomes. *J Biol Chem* 267: 22243-22248.
755 66. Rytömaa M, Kinnunen PK (1994) Evidence for two distinct acidic phospholipid-
756 binding sites in cytochrome *c*. *J Biol Chem* 269: 1770-1774.
757 67. Sinibaldi F, *et al.* (2008) Insights into cytochrome *c*-cardiolipin interaction. Role
758 played by ionic strength. *Biochemistry* 47: 6928-6935.
759 68. Kawai C, *et al.* (2005) pH-Dependent interaction of cytochrome *c* with mitochondrial
760 mimetic membranes: the role of an array of positively charged amino acids. *J Biol*
761 *Chem* 280: 34709-34717.
762 69. Guerra-Castellano A, Díaz-Moreno I, Velázquez-Campoy A, De la Rosa MA, Díaz-
763 Quintana A (2016) Structural and functional characterization of phosphomimetic
764 mutants of cytochrome *c* at threonine 28 and serine 47. *Biochim Biophys Acta –*
765 *Bioenerg* 1857: 387-395.
766 70. Serpas L, Milorey B, Pandiscia LA, Addison AW, Schweitzer-Stanner R (2016)
767 Autoxidation of reduced horse heart cytochrome *c* catalyzed by cardiolipin-
768 containing membranes. *J Phys Chem B* 120: 12219-12231.
769 71. Hanske J, *et al.* (2012) Conformational properties of cardiolipin-bound cytochrome
770 *c*. *Proc Natl Acad Sci USA* 109: 125-130.
771 72. Pandiscia LA, Schweitzer-Stenner R (2015) Coexistence of native-like and non-
772 native partially unfolded ferricytochrome *c* on the surface of cardiolipin-containing
773 liposomes. *J Phys Chem B* 119: 1334-1349.

774 73. Pandiscia LA, Schweitzer-Stenner R (2015) Coexistence of native-like and non-
775 native cytochrome *c* on anionic liposomes with different cardiolipin content. *J Phys*
776 *Chem B* 119: 12846-12859.
777 74. Domanov YA, Molotkovsky JG, Gorbenko GP (2005) Coverage-dependent changes
778 of cytochrome *c* transverse location in phospholipid membranes revealed by FRET.
779 *Biochim Biophys Acta – Biomembr* 1716: 49-58.
780 75. Assfalg M, *et al.* (2003) Structural model for an alkaline form of ferricytochrome *c*. *J*
781 *Am Chem Soc* 125: 2913-2922.
782 76. Kagan VE, *et al.* (2006) The "pro-apoptotic genies" get out of mitochondria: oxidative
783 lipidomics and redox activity of cytochrome *c*/cardiolipin complexes. *Chem Biol*
784 *Interact* 163: 15-28.
785 77. Ameri K, *et al.* (2015) HIGD1A regulates oxygen consumption, ROS production, and
786 AMPK activity during glucose deprivation to modulate cell survival and tumor growth.
787 *Cell Rep* 10: 891-899.
788 78. An HJ, *et al.* (2011) The survival effect of mitochondrial *Higd-1a* is associated with
789 suppression of cytochrome *c* release and prevention of caspase activation. *Biochim*
790 *Biophys Acta – Mol Cell Res* 1813: 2088-2098.
791 79. Schimada S, *et al.* (2017) Complex structure of cytochrome *c*-cytochrome *c* oxidase
792 reveals a novel protein-protein interaction mode. *EMBO J* 36: 291-300.
793 80. Yu H, Lee I, Salomon AR, Yu K, Hüttemann M (2008) Mammalian liver cytochrome
794 *c* is tyrosine-48 phosphorylated *in vivo*, inhibiting mitochondrial respiration. *Biochim*
795 *Biophys Acta – Biomembr* 1777: 1066-1071.
796 81. Blouin C, Guillemette JG, Wallace CJA (2001) Resolving the individual components
797 of a pH-induced conformational change. *Biophys J* 81: 2331-2338.
798 82. Gu J, *et al.* (2016) The architecture of the mammalian respirasome. *Nature* 537:
799 639-643.
800 83. Letts JA, Fiedorczuk K, Sazanov LA (2016) The architecture of respiratory
801 supercomplexes. *Nature* 537: 644-648.

802

FIGURE LEGENDS

Figure 1. Control of human cell fate by C*c*-based signalosome, and biophysical and structural characterization of the Y48*p*CMF variant of C*c*. (a) Diagram of the role of C*c* in homeostasis and apoptosis. *Left*, Under homeostatic conditions, C*c* (red circles) transfers electrons from cytochrome bc_1 complex (Cbc_1) to cytochrome *c* oxidase complex (C*c*O). *Right*, Upon apoptotic stimuli, C*c* is released to the cytosol to induce apoptosome formation and block pro-survival pathways. A portion of C*c* remains bound to cardiolipin (CL). **(b)** Far-UV CD spectra of the reduced forms of WT (blue) and Y48*p*CMF C*c* (red). The same color-code is maintained in the following panels. **(c)** Superimposition of the $^{1}H–^{15}N$ HSQC spectra of uniformly ^{15}N-labeled forms of WT and Y48*p*CMF C*c*. Backbone amide resonances of Y48*p*CMF C*c* are labelled in red and black. Particular amide resonances of WT C*c* are labelled in blue. **(d)** Detailed view of the ^{1}H NMR spectra of WT and Y48*p*CMF C*c* at negative ppm values. Resonances for Met80 side-chain protons are shown for both C*c* species. Assigned signals of all residues within this region are displayed for Y48*p*CMF C*c*. The extra signal of WT C*c* corresponds to the $Q\delta_1$ protons of Ile53. **(e)** Superimposition of the aromatic region of the $^{1}H–^{13}C$ HSQC spectra of WT and Y48*p*CMF C*c* acquired in ^{13}C natural abundance. Assigned aromatic resonances of Y48*p*CMF C*c* are displayed in red.

Figure 2. NMR solution structure of the Y48*p*CMF variant of C*c*. (a) Stereo-view ribbon representation of the 20 best conformers of Y48*p*CMF C*c*. Heme group atoms are displayed for all conformers. Ribbons are colored in red, whereas atoms from the heme group are colored following the CPK color scheme. Foldons of Y48*p*CMF C*c* are shadowed and marked with Roman numerals, except for foldon III, which is located behind foldon IV. **(b)** Comparison between the NMR solution structures of WT C*c* (PDB ID: 1J3S) (33) and Y48*p*CMF C*c* (this work). The ribbon for WT C*c* is in blue. The five α-helices of both C*c* species, as well as the mutation-containing

loop of Y48*p*CMF C*c*, are marked. Arrows point to the regions on the Y48*p*CMF C*c* ribbon with substantial structural changes as compared to the WT form. **(c)** Detailed view of the loop harboring the pCMF48 residue. *p*CMF48 atoms follow the CPK color scheme. Protein structures were represented with the UCSF Chimera software (40). **(d)** Detail of the heme group and axial ligands. Labels display iron-to-axial ligand distances for the Y48*p*CMF mutant obtained from the EXAFS analysis (see **Figure S5**).

Figure 3. Relaxation NMR measurements and dynamic properties of WT and Y48*p*CMF C*c*. (a–c) Differences in Heteronuclear NOE **(a)**, relaxation rate R_1 **(b)** and relaxation rate R_2 **(c)** between the experimental values for the reduced forms of WT and Y48*p*CMF C*c*, plotted as a function of the residue number. Gaps in data result from overlapping resonances, broadened resonances beyond the detection limit and unassigned resonances. A scheme of the secondary structure elements is included at the top of each plot. **(d)** Map of the Y48*p*CMF C*c* residues colored according to their dynamic properties. Affected residues in the heteronuclear NOE and relaxation rate R_2 parameters are colored in yellow and orange, respectively. Residues with backbone amide resonances that are undetectable in the $^{1}H–^{15}N$ HSQC spectrum of Y48*p*CMF C*c* but detectable in the $^{1}H–^{15}N$ HSQC spectrum of WT C*c* are colored in red. *p*CMF48 is shown in black and the heme group, in green. Unaffected, unassigned and proline residues are in blue. **(e)** Internal mobility comparison between Y48*p*CMF and WT C*c*. S^2 order parameter values per residue for Y48*p*CMF (*upper*) and WT (*lower*) C*c* are represented on the respective NMR ribbon structures using a blue-red scale. Undetectable backbone resonances are in gray. Heme atoms are in green with the axial ligands depicted in sticks.

Figure 4. Binding assays between Y48*p*CMF C*c* and its respiratory partners. **(a)** Overlay of selected residues of $^{1}H–^{15}N$ HSQC spectra of ^{15}N-labeled Y48*p*CMF

C*c* along with titration with Cc_1. Signals corresponding to different titration steps are colored according to the code indicated in the panel. **(b)** Plot of chemical-shift perturbations (CSPs) of ^{15}N-labeled Y48*p*CMF C*c* as a function of residue number. Proline and non-assigned residues are marked by asterisks. Color bars stand for the $\Delta\delta_{avg}$ categories, as follows: insignificant $\Delta\delta_{avg} < 0.025$ ppm, blue; small $0.025 \leq \Delta\delta_{avg} < 0.050$ ppm, yellow; medium $0.050 \leq \Delta\delta_{avg} < 0.075$ ppm, orange; and large ≥ 0.075 ppm, red. **(c)** *Upper*, curves representing the best global fit of several amide signals in ^{1}H dimension to a 2:1 ratio for the Y48*p*CMF C*c*-Cc_1 binding model with two different global K_D values. *Lower*, binding curves of Gln16. Lines represent the best fit to 1:1 (red) and 2:1 (black) binding models. **(d)** CSP map of reduced Y48*p*CMF C*c* upon addition of reduced Cc_1 at a 1:1 ratio. Residues are colored according to the $\Delta\delta_{avg}$ categories, as indicated in (b). Proline and non-assigned residues are in gray. **(e)** ITC measurements of the Y48*p*CMF C*c*-Cc_1 and Y48*p*CMF C*c*-C*c*O complexes in their reduced states. Experimental data were fitted to a 2:1 binding model. Thermograms are shown in the *upper* panels, and binding isotherms, in the *lower* panels.

Figure 5. C*c*O activity with WT or Y48*p*CMF C*c* as the electron donor. (a) C*c*O activity of isolated complex IV and of mitochondria lacking C*c* (ΔC*c*) upon addition of exogenous WT (blue bars) or Y48*p*CMF C*c* (red bars). Western blot results confirmed the lack of endogenous C*c* in ΔC*c* mitochondria (see *inset*). **(b)** *In vitro* modulation of C*c*O activity by HIGD1A and HIGD2A. WT C*c* (blue bars) or Y48*p*CMF C*c* (red bars), along with HIGD1A or HIGD2A at the indicated ratios, were added to isolated complex IV. **(c)** Effect of the modulators Rcf1 and Rcf2 on the C*c*O activity of mitochondria isolated from yeasts grown in YPD or YP-Gal media with either WT C*c* (blue bars) or Y48*p*CMF C*c* (red bars). All data represent the mean ± SD of three independent experiments. In all cases, C*c*O activity was detected only upon addition of exogenous C*c* but not with endogenous C*c*. *Inset*, Western blots of WT_{Rcf}

887 mitochondria (lane 1) and mitochondria lacking Rcf1 and Rcf2 (ΔRcf1/2) (lane 2).
888 **(d)** Blue-native gel (BN-PAGE) and Western blots of mitochondria from WT_{Rcf} and
889 ΔRcf1/2 strains, using antibodies against Rcf2 and COX-II. Bands submitted to
890 tryptic digestion (**Figure S11d**) are highlighted by asterisks. **(e)** Scheme of the
891 interactions within the electron transport chain involving C*cb*$_1$, C*c*O, Rcf proteins and
892 WT or Y48*p*CMF C*c*, as a function of glucose (Glu) availability. The Rcf proteins
893 facilitate the interaction between C*cb*$_1$ and C*c*O to form OxPhos supercomplexes,
894 mainly under glucose deprivation (*right*). Thickness of solid arrows refers to the
895 electron transfer rate at the C*c*-binding proximal sites of C*bc*$_1$ and C*c*O by WT or
896 Y48*p*CMF C*c*—the longer and thicker the arrow, the more efficient the electron
897 transfer. Dashed line highlights the channeling of WT C*c* molecules.
898
899 **Figure 6. Liposome-binding assays with caspase-3 activity induced by WT and**
900 **Y48*p*CMF C*c*. (a,b)** Electrophoretic mobility shift assay (EMSA) of C*c* in the
901 presence of increasing concentrations of lipids. DOPC:TOCL (4:1) or DOPC
902 liposomes were incubated with WT **(a)** or Y48*p*CMF **(b)** C*c*. Note that free C*c*
903 species moved to the cathode, whereas liposome-bound C*c* migrated to the anode.
904 Lanes marked by rectangles correspond to the C*c*:lipid ratio at which the peroxidase
905 activity was determined (see *below*). **(c)** Calorimetric assays for lipid binding to C*c*.
906 *Upper*, ITC thermograms, corresponding to titrations of DOPC:TOCL 4:1 liposomes
907 (black), WT C*c* (blue) or Y48*p*CMF C*c* (red). *Lower*, binding isotherms with WT C*c*
908 (blue dots) or Y48*p*CMF C*c* (red dots). Continuous lines represent the best fits to a
909 sequential binding, as computed with the Nanoanalyze software (TA instruments)
910 with a stoichiometry of 30 molecules of lipid per molecule of C*c*. **(d)** Relative
911 peroxidase activities of WT C*c* (blue) or Y48*p*CMF C*c* (red) in the presence of
912 liposomes containing DOPC (empty bars) or DOPC:TOCL (4:1) 901 (filled bars). **(e)**
913 Relative caspase-3 activity in HEK293 cell extracts devoid of endogenous C*c* upon
914 addition of exogenous WT C*c* (blue) or Y48*p*CMF C*c* (red). A lack of caspase auto-

activation was verified in a run without the addition of C*c* (gray). Western blots confirmed the lack of endogenous C*c* in cytoplasmic cell extracts after immunoblotting with anti α-tubulin (cytosolic marker) and anti-C*c* antibodies (see *inset*). Lane 1, cytoplasmic cell extracts; lane 2, C*c*; lane 3, BSA as a negative control.

Figure 7. Schematic diagram illustrating the changes induced in cell function by phosphomimic Y48*p*CMF C*c*. The negative charge at position 48 decreases C*c*O activity by disrupting C*c* channeling in OxPhos supercomplexes (*left*), enhances ROS scavenger activity by increasing the peroxidase activity of CL-bound C*c* (*middle*) and promotes the anti-apoptotic function of Y48*p*CMF C*c* by inhibiting its ability to activate the caspase-3 cascade (*right*).

Structural Basis of Mitochondrial Dysfunction in Response to Cytochrome *c* Phosphorylation at Tyrosine 48

Supplementary Information

Blas Moreno-Beltrán[1,*], Alejandra Guerra-Castellano[1,*], Antonio Díaz-Quintana[1], Rebecca Del Conte[2], Sofía M. García-Mauriño[1], Sofía Díaz-Moreno[3], Katiuska González-Arzola[1], Carlos Santos-Ocaña[4], Adrián Velázquez-Campoy[5], Miguel A. De la Rosa[1], Paola Turano[2] and Irene Díaz-Moreno[1,#]

[1]Instituto de Investigaciones Químicas, cicCartuja, Universidad de Sevilla – CSIC, Avda. Américo Vespucio 49, 41092 Seville (Spain).

[2]Magnetic Resonance Center (CERM) – Department of Chemistry, University of Florence, Via Luigi Sacconi 6, 50019 Sesto Fiorentino, Florence (Italy).

[3]Diamond Light Source Ltd., Harwell Science and Innovation Campus, Didcot, Oxfordshire OX11 0DE (United Kingdom).

[4]Centro Andaluz de Biología del Desarrollo, Universidad Pablo de Olavide – CSIC, and CIBERER Instituto de Salud Carlos III, Carretera de Utrera km. 1, 41013 Seville (Spain).

[5]Institute of Biocomputation and Physics of Complex Systems (BIFI), Joint Unit BIFI-IQFR (CSIC), Universidad de Zaragoza, Mariano Esquillor s/n, 50018 Zaragoza (Spain); Aragon Institute for Health Research (IIS Aragon), Avda. San Juan Bosco 13, 50009 Zaragoza, Spain; Fundacion ARAID, Government of Aragon, Maria de Luna 11, 50018 Zaragoza (Spain).

*These authors contribute equally to the work.

[#]Correspondence should be addressed to I. D.-M. (idiazmoreno@us.es)

Telephone number: +34 954489513; Fax number: +34 954460065

SUPPLEMENTARY METHODS

Protein expression and purification

Uniformly ^{13}C,^{15}N-labeled, ^{15}N-labeled and unlabeled samples of the Y48*p*CMF variant species of cytochrome *c* (C*c*)—in which tyrosine 48 was replaced by *p*-carboxymethyl-L-phenylalanine (*p*CMF)—were expressed using the evolved tRNA synthetase technique and purified as previously described (1, 2). For isotopic labelling, ^{15}N-labeled ammonium chloride and ^{13}C-labeled glucose were added to minimal cell culture media to express the ^{13}C,^{15}N-labeled protein samples, whereas only ^{15}N-labeled ammonium chloride was added to media for ^{15}N-labeled protein samples. Unlabeled *p*CMF and δ-aminolevulinic acid were added to a final concentration of 1 mM each after cell culture induction. Cultures were induced with IPTG and arabinose at 1 mM and 0.02% final concentrations, respectively. Tryptic digestion and MALDI-TOF analyses confirmed the molecular mass and the substitution of tyrosine by *p*CMF. Uniformly ^{15}N-labeled and unlabeled samples of wild-type (WT) C*c* were expressed and purified as reported previously (3). Protein concentration was determined by visible spectrophotometry, using an extinction coefficient of 29 mM^{-1} cm^{-1} for reduced Y48*p*CMF and WT C*c.* For NMR experiments, pure C*c* samples were first dialyzed against 10 mM sodium phosphate (pH 6.3), and afterwards concentrated in Millipore 3 K Nominal Molecular Weight Limit (NMWL) centricons until a final C*c* concentration of 0.7 mM.

Plant cytochrome c_1 (Cc_1) was obtained as described (4). Bovine cytochrome *c* oxidase (C*c*O) was purchased from Sigma; before use, the buffer was exchanged to 10 mM sodium phosphate buffer (pH 7.4), supplemented with 0.2% (w/v) *n*-dodecyl-β-D-maltoside (DDM) and 5 mM sodium dithionite, using Millipore 3K NMWL centricons, as reported previously (3).

Hypoxia-inducible domain family members 1A and 2A (HIGD1A and HIGD2A, respectively) were expressed by cell-free protein synthesis using a continuous exchange reaction

(dialysis mode; ratio 1:10), with a 6 mL final volume. Briefly, 10 μg mL^{-1} of either HIGD1A or HIGD2A-coding DNA in the pIVEX2.4d plasmid were added to the reaction mixture, which consisted of 1 mM amino acid mix, 0.8 mM ribonucleotides (guanosine-, uracyl- and cytidine-triphosphate), 1.2 mM adenosine triphosphate, 55 mM HEPES buffer (pH 7.5), 68 μM folinic acid, 0.64 mM cyclic adenosinemonophosphate, 3.4 mM dithiothreitol, 27.5 mM ammonium acetate, 2 mM spermidine, 80 mM creatine phosphate, 208 mM potassium glutamate, 16 mM magnesium acetate, 250 μg mL^{-1} of creatine kinase, 27 μg mL^{-1} of T7 RNA polymerase, 0.175 μg mL^{-1} of tRNA and 0.4 mL of S30 *Escherichia coli* (*E. coli*) bacterial extract. DDM detergent was added to a final concentration of 0.4% (w/v). For the feeding mix in the external tank (60 mL), the same conditions were used but omitting DNA, creatine kinase, T7 RNA polymerase, tRNA and S30 *E. coli* bacterial extract. Incubation was carried out at 23°C with agitation for 16 h. The His-tagged forms of HIGD1A and HIGD2A were then purified by nickel affinity chromatography. The final yield was 125 μg of protein per mL of reaction in both cases. Before using the HIGD proteins, the buffers were exchanged to 10 mM sodium phosphate buffer (pH 7.4) with 0.2% (w/v) DDM.

Circular dichroism

Circular dichroism (CD) spectra were recorded on a JASCO J-815 spectropolarimeter, equipped with a Peltier temperature system, in a 1-mm quartz cuvette. CD intensities were presented in terms of molar ellipticity [θ_{molar}], based on molar protein concentration (5). Secondary structural elements of reduced WT and Y48*p*CMF C*c* were analyzed by recording their respective far-UV CD spectra (185–250 nm) at 25°C. The samples contained 3 μM hemeprotein in 5 mm sodium phosphate buffer (pH 6.3), supplemented with 10 mM ascorbic acid. Twenty scans were averaged and analyzed for each sample, using the CDPro

software package (6, 7) SMP50 and SP37A were used as reference sets. CLSTR option was employed for comparison with a set of proteins with similar folds.

Nuclear magnetic resonance experiments

Nuclear magnetic resonance (NMR) spectra of fresh 0.6 mM reduced ^{13}C,^{15}N-labeled Y48*p*CMF C*c* samples, in 90% buffer and 10% D_2O, were recorded at 25 °C on Bruker Avance spectrometers operating at 950, 700 and 500 MHz ^{1}H frequencies. A standard set of triple-resonance experiments, necessary for the full assignment of backbone and side-chain resonances, were acquired at 700 MHz ^{1}H frequency, whereas 2D and 3D NOESY experiments required for structure determination were acquired at 950 MHz ^{1}H frequency. Recorded NMR experiments for determination of backbone resonances were 2D ^{1}H-^{15}N heteronuclear single-quantum correlation (HSQC), 2D ^{1}H-^{13}C HSQC, 3D HNCA, 3D HNCACB, 3D CACB(CO)NH, 3D HN(CA)CO and 3D HNCO, and specific experiments for determination of side-chain resonances were 3D HCCHTOCSY and 3D HBHA(CO)NH (8-10). Additional 2D COSY and aromatic 2D ^{1}H-^{13}C HSQC spectra of an unlabeled sample of Y48*p*CMF C*c* were acquired for the assignment of aromatic residues. Therefore, the ^{1}H-^{13}C HSQC spectrum was recorded in natural abundance of ^{13}C. Water suppression was achieved in all mentioned spectra by WATERGATE (11) 1D ^{1}H spectra were launched before and after each spectrum to check the state of the sample, and especially the redox state of the hemeprotein.

The following NOESY experiments were acquired: 2D ^{1}H-^{15}N NOESY, 3D ^{1}H-^{15}N NOESY-HSQC and 3D ^{1}H-^{13}C NOESY-HSQC spectra in the aliphatic region (12-14). Mixing times were 100 ms for all NOESY experiments, recorded on a ^{15}N-labeled sample, with the exception of the 3D ^{1}H-^{13}C NOESY-HSQC, which was acquired on a ^{13}C,^{15}N-labeled sample. An additional 2D ^{1}H-^{15}N EXSY spectrum was launched for assignment of heme resonances

using a partially oxidized ^{15}N-labeled sample. WATERGATE suppression was used. 1D ^{1}H spectra were again launched to check the state of the samples.

^{15}N relaxation R_1 (=1/T_1), R_2 (=1/T_2) and {^{1}H}-^{15}N NOE parameters (also known as HetNOE) were obtained from standard experiments recorded at 500 MHz ^{1}H frequency and 25 °C (15) on ^{15}N-labeled samples of the Y48*p*CMF and WT C*c* species. R_1 and R_2 values were obtained using 10 delays, of 1, 2.5, 10, 35, 70, 200, 380, 550, 740 and 3000 ms for R_1 experiments, and 16.96, 33.92, 67.84, 101.76, 135.68, 186.56, 237.44, 271.36, 305.28 and 356.16 ms for R_2 experiments. To determine HetNOE values, spectra were recorded in the presence or absence of a proton presaturation period. HetNOE, R_1 and R_2 values from residues in well-defined regions were used to estimate the comprehensive ^{15}N relaxation parameters (16, 17). The R_1/R_2 ratio was used to estimate the rotational correlation time (τ_c) of the protein constructs using TENSOR2 software (17). Internal mobility was also calculated by an isotropic model-free analysis via TENSOR2 routines (17). Amide hydrogen exchange experiments were also carried out on these ^{15}N-labeled samples of the Y48*p*CMF and WT C*c* species. For this purpose, 2D ^{1}H-^{15}N HSQC experiments were run using C*c* samples in 95% buffer and 5% D_2O, or 100% D_2O.

NMR data processing was carried out using the Bruker TopSpin software package. The assignments of 2D and 3D spectra were performed manually with the help of the CARA and SPARKY software packages (18, 19). A list of NOEs of reduced yeast C*c* was used as a reference (20). Final reviews of peak assignments and integrations of peak volumes were executed by the XEASY software (21). ^{15}N relaxation parameters were analyzed using CARA routines (19).

NMR titrations of 100 μM ^{15}N-labeled, reduced Y48*p*CMF C*c* with aliquots of unlabeled, reduced plant cytochrome c_1 (Cc_1) were performed at 25ºC and recorded on a Bruker Avance 700 MHz. Titrations were performed in 5 mM sodium phosphate (pH 6.3) with 10%

D_2O. Each titration step was prepared in an independent NMR tube (Shigemi) up to a 0.28 mL final volume. The pH of the samples was checked before and after recording each spectrum. The Chemical-Shift Perturbations (CSP) were monitored in a series of ^{1}H-^{15}N HSQC experiments. The data were processed using Bruker TopSpin and analyzed with SPARKY (18). CSP titration curves were analyzed with Origin 7 (OriginLab, http://www.originlab.com), using a two-parameter non-linear least squares fit with two-site binding model, as previously described (3, 4).

Distance geometry calculations

Volumes of cross-peaks between assigned resonances were obtained using the integration routines of the XEASY program. Elliptical integration was applied. NOESY cross-peak intensities were converted into upper limits of inter-atomic distances by CYANA (22). The heme group, axial ligands and two Cys residues covalently linked to the porphyrin ring were treated as in previous computations (23). Upper and lower distance limits were imposed to build up the heme group. Upper (1.90 Å) and lower (1.70 Å) distance limits from the α-carbons of thioethers 2 and 4 of the heme moiety to the S_γ of cysteines 14 and 17, respectively, were used in the computations to covalently link the heme moiety to the cysteine residues. An upper distance limit of 2.50 Å and a lower distance limit of 2.20 Å between the S_δ of Met80 and the heme iron atom were also introduced. The orientations of Met80 and His18 side-chains were defined only by experimental NOE constraints.

A residue containing the heme moiety was added to the standard CYANA library. In addition, the non-standard amino acid *p*CMF was built and added to the CYANA library. Several cycles of structure calculation were carried out in order to recalibrate the NOE distance constraints. CYANA calculations were performed following the procedure and with the parameters used for the determination of other *c*-type cytochromes (20, 24, 25). Initially, 200

structures were calculated. In each calculation, violated constraints were analyzed for the 20 best structures with respect to the target function. After consecutive rounds of review and refinement of violated constraints, a final CYANA computation was performed in which no consistent violations were determined. The final average value of the target function was equal to 0.73 ± 018.

Molecular dynamics simulations

NMR-restrained Molecular Dynamics (RMD) computations were performed by the AMBER 12.1 package and using the AMBER-2003 force field on a selection of the 20-best structures derived from the CYANA calculations (26, 27). Distance constraints were introduced by the DIS_RST module of Amber 12.1. Simulations were performed under periodic boundary conditions using an orthorhombic cell geometry (with the minimum distance between protein and cell faces initially set to 10 Å) and particle mesh Ewald (PME) electrostatics with a Ewald summation cut off of 9 Å. The structures were solvated with extended simple point charge model (SPC) water molecules, and Cl^- counterions were added to neutralize the net charge of the full systems. Afterwards, solvent and counterions were subjected to 2500 steps of steepest descent minimization followed by 500 ps NPT-MD computations using isotropic molecule position scaling and a pressure relaxation time of 2 ps at 298 K. Once the systems were NMR-restrained energy minimized (REM), the resulting data were submitted to RMD computations for 5 ns at 298 K. The temperature was regulated using a Langevin thermostat with a collision frequency of 5 ps^{-1} (28). Finally, structures from RMD were energy minimized for 5000 steps. The SHAKE algorithm was used to constrain bonds involving hydrogen atoms (29). The PTRAJ module of AMBER was used for trajectory analyses. Force field parameters for the heme group were taken from a previous work (30). The Met80 residue was non-bonded to the iron atom and a constraint was applied instead. Molecular graphics

were performed with UCSF Chimera (31). Final minimized structures were validated by the Protein Structure Validation Software suite (PSVS) (32), the iCING server (33) and the Protein Data Bank (PDB) validation suite. In addition, a non-restrained MD computation of 20 ns was launched to check the stability of the resulting conformers. A non-restrained MD computation of 20 ns was also launched on the NMR structure of WT C*c*. S^2 parameters values per residue were obtained from the non-restrained computations performed for both C*c* species.

Finally, NMR assignments and PDB coordinates for the Y48*p*CMF C*c* were deposited in the Biological Magnetic Resonance Data Bank (BMRB) and PDB databases. BMRB and PDB entries for the Y48*p*CMF C*c* are 25660 and 2N3Y, respectively.

X-ray absorption spectroscopy

X-ray absorption spectroscopy (XAS) experiments were carried out at Diamond Light Source (UK), operating at 3 GeV and 300 mA ring current. The Fe K-edge (7112 eV) was measured at beamline I20-scanning, comprising a four-bounce Si(111) crystal monochromator. Two Rh-coated mirrors working at 5.0 mrad were used for high-energy harmonics rejection. The spectra were recorded in fluorescence mode, using a 36-element monolithic Ge detector (Canberra). An iron foil was simultaneously recorded in transmission mode using ionization chamber detectors to be used as internal calibration. To avert radiation damage, X-rays were attenuated with a 1.5-mm thick carbon foil. In addition, samples were measured at cryogenic temperatures using a liquid nitrogen cryojet (Oxford Instrument). Each datapoint was collected using a 1 s acquisition time, and 36 scans were averaged. Samples were measured in plastic capillary cells. 350 μM reduced C*c* samples were prepared in 10 mM sodium phosphate buffer (pH 5.8).

Spectra averaging, background subtraction and amplitude normalization required to obtain the extended X-ray absorption fine structure (EXAFS) signals (k) were performed using the Athena (version 0.9.024) code (34). The best fit to the data was performed by using the Artemis program (version 0.9.024) (34). Scattering paths were computed using FEFF 6.0. Initial atomic coordinates of the heme moiety were taken from the crystallographic structure of the WT form (PDB: 3zcf) (35). Neither the initial coordinates from this structure nor those from the NMR structure (PDB: 1j3s) (36) yielded acceptable fits. Still, the distances coming out from these fits were used as input to screen 10^4 coordinates from each MD computation (2). The snapshots with the smallest sum of quadratic distance differences with respect to the EXAFS fit-derived distances were selected iteratively.

Isothermal titration calorimetry

Interactions of the human C*c* species with plant Cc_1, at their reduced and oxidized states were analyzed by isothermal titration calorimetry (ITC) using an Auto-ITC200 microcalorimeter (MicroCal) at 25 °C. The reference cell was filled with distilled water. The experiments consisted of 2 μL injections of 0.4 mM C*c* solution in 10 mM sodium phosphate buffer (at pH 5.8, 7.4 and 8.5) into the sample cell, initially containing 20 μM Cc_1 solution in the same buffer. All solutions were degassed before titration. Titrant was injected at appropriate time intervals to ensure that the thermal power signal returned to the baseline prior to the next injection. To achieve a homogeneous mixing in the cell, the stirring speed was kept constant at 1000 rpm. The data, specifically the heat-per-injection normalized per mol of injectant *versus* molar ratio, were analyzed with Origin 7 (OriginLab) using a two-site binding model with a distinct affinity for each site, as recently reported for the plant C*c*-Cc_1 complex (4). In addition, the titration of reduced bovine C*c*O (3.85 μM) with the reduced C*c* species (0.10 mM) was performed in 10 mM sodium phosphate buffer (pH 7.4),

supplemented with 0.2% (w/v) *n*-dodecyl-β-D-maltoside and 5 mM sodium dithionite, as described previously (3). ITC experiments were repeated at least twice to confirm that the data were consistent. The titration of C*c* onto buffer containing detergent yielded small invariable injection heats attributed to dilution. Calibration and performance tests of the calorimeter were carried out by conducting Ca^{+2}-EDTA titrations with the solutions provided by the manufacturer.

ITC assays were analyzed considering several models: single binding site, two identical independent binding sites and two different independent binding sites.

Single binding site

A single binding site for C*c* is considered in Cc_1 (or C*c*O). The total concentration of C*c* and Cc_1 (or C*c*O) in the cell after injection *i* was calculated as:

$$[\mathrm{C}c]_{T,i} = [\mathrm{C}c]_0 \left(1 - \left(1 - \frac{v}{V_0}\right)^i\right)$$

$$[\mathrm{C}c1]_{T,i} = [\mathrm{C}c1]_0 \left(1 - \frac{v}{V_0}\right)^i$$

where $[\mathrm{C}c]_0$ and $[\mathrm{C}c_1]_0$ are the concentrations of C*c* in the syringe and the initial concentration of Cc_1 (or C*c*O) in the cell, v is the injection volume, and V_0 is the cell volume. Mass conservation principle and chemical equilibrium allow writing a set of coupled equations for C*c* and Cc_1 (or C*c*O):

$$[\mathrm{C}c]_T = [\mathrm{C}c] + [\mathrm{C}c1{:}\,\mathrm{C}c] = [\mathrm{C}c] + K_A[\mathrm{C}c1][\mathrm{C}c]$$
$$[\mathrm{C}c1]_T = [\mathrm{C}c1] + [\mathrm{C}c1{:}\,Cc] = [\mathrm{C}c1] + K_A[\mathrm{C}c1][Cc]$$

where K_A is the equilibrium association constant for the complex Cc_1:C*c* (or C*c*O:C*c*). These two equations can be transformed into a single equation in [C*c*]:

$$[\mathrm{C}c]_T = [\mathrm{C}c] + [\mathrm{C}c1]_T \frac{K_A[\mathrm{C}c]}{1 + K_A[\mathrm{C}c]}$$

which is a quadratic polynomial equation that can be solved at each experimental point in the calorimetric titration in order to find the concentration of free C*c*. Then, the concentration of complex Cc_1:C*c* (or C*c*O:C*c*) after each injection can be calculated:

$$[\mathrm{C}c1{:}\,\mathrm{C}c] = [\mathrm{C}c1]_T \frac{K_A[\mathrm{C}c]}{1 + K_A[\mathrm{C}c]}$$

Finally, the titrant-normalized heat effect associated with each injection *i* can be calculated from the net increase of complex Cc_1:C*c* (C*c*O:C*c*) or concentration along injection *i*:

$$q_i = \frac{V_0}{v[\mathrm{C}c]_0}\Delta H\left([\mathrm{C}c1{:}\,Cc]_i - [\mathrm{C}c1{:}\,Cc]_{i-1}\left(1 - \frac{v}{V_0}\right)^i\right) + q_d$$

where ΔH is the interaction enthalpy, and q_d is an additional parameter accounting for the background (or dilution) heat. Non-linear least-square regression analysis of the experimental data using the previous equation provides an estimation of the binding parameters.

Two independent binding sites

Two independent binding sites for C*c* are considered in in Cc_1 (or C*c*O). The total concentration of C*c* and in Cc_1 (or C*c*O) in the cell after injection *i* was calculated as:

$$[\mathrm{C}c]_{T,i} = [\mathrm{C}c]_0\left(1 - \left(1 - \frac{v}{V_0}\right)^i\right)$$

$$[\mathrm{C}c1]_{T,i} = [\mathrm{C}c1]_0\left(1 - \frac{v}{V_0}\right)^i$$

where [C*c*]$_0$ and [Cc_1]$_0$ are the concentration of Cc in the syringe and the initial concentration of Cc_1 (or C*c*O) in the cell, v is the injection volume, and V_0 is the cell volume. Mass conservation principle and chemical equilibrium allow writing a single equation in [C*c*]:

$$[\mathrm{C}c]_T = [\mathrm{C}c] + [\mathrm{C}c1]_T\left(\frac{K_{A1}[\mathrm{C}c]}{1 + K_{A1}[\mathrm{C}c]} + \frac{K_{A2}[\mathrm{C}c]}{1 + K_{A2}[\mathrm{C}c]}\right)$$

where K_{A1} and K_{A2} are the equilibrium association constants for the complexes Cc_1:C*c* (or C*c*O:C*c*) and C*c*:Cc_1 (or C*c*:C*c*O). This is a cubic polynomial equation that can be solved (numerically) at each experimental point in the calorimetric titration in order to find the

concentration of free C*c*. Then, the concentration of complexes Cc_1:C*c* (or C*c*O:C*c*) and C*c*:Cc_1 (or C*c*:C*c*O) after each injection can be calculated:

$$[\mathrm{C}c1{:}\,\mathrm{C}c] = [\mathrm{C}c1]_T \frac{K_{A1}[\mathrm{C}c]}{1 + K_{A1}[\mathrm{C}c]}$$

$$[\mathrm{C}c{:}\,\mathrm{C}c1] = [\mathrm{C}c1]_T \frac{K_{A2}[\mathrm{C}c]}{1 + K_{A2}[\mathrm{C}c]}$$

Finally, the titrant-normalized heat effect associated with each injection *i* can be calculated from the net increase of complexes Cc_1:C*c* (or C*c*O:C*c*) and C*c*:Cc_1 (or C*c*:C*c*O) concentration along injection *i*:

$$q_i = \frac{V_0}{v[\mathrm{C}c]_0}\left(\Delta H_1\left([\mathrm{C}c1{:}\,\mathrm{C}c]_i - [\mathrm{C}c1{:}\,\mathrm{C}c]_{i-1}\left(1 - \frac{v}{V_0}\right)^i\right)\right.$$

$$\left. + \Delta H_2\left([\mathrm{C}c{:}\,\mathrm{C}c1]_i - [\mathrm{C}c{:}\,\mathrm{C}c1]_{i-1}\left(1 - \frac{v}{V_0}\right)^i\right)\right) + q_d$$

where ΔH_1 and ΔH_2 are the interaction enthalpies for each binding site. Non-linear least-square regression analysis of the experimental data using the previous equation provides estimates of the binding parameters.

This model corresponds to *two identical independent binding sites* when it is imposed that $K_{A1} = K_{A2}$ and $\Delta H_1 = \Delta H_2$.

C-values calculated using the K_D values of the *proximal* site in the Y48*p*CMF C*c*-involving titrations (Tables S5 and S6) are in the range of values allowed ($1 < C < 1000$).

Calorimetric liposome binding assays were carried out in a low-volume Nano-ITC (TA instruments, Inc.). All titrations were performed in 25 mM HEPES buffer (pH 7.4). A 6 μM C*c* solution, previously reduced by an excess of sodium ascorbate that was further removed by dialysis, was titrated with a suspension of unilamellar liposomes. Stirring was set to 350 rpm. Unilamellar liposomes contained 1,2-dioleoyl-*sn*-glycero-3-phosphocholine (DOPC) either alone or with 1,1'2,2'-tetraoleoylcardiolipin (TOCL) at a 4:1 ratio. Total lipid concentration in

the syringe was 8.9 mM. DOPC unilamellar liposomes (7.9 mM) were used for control experiments. All ITC samples were previously degassed allowing C*c* species to remain reduced in the syringe. In addition, C*c*-liposome binding assays were performed under aerobic conditions, as reported in ref. (37). In such binding assays, each liposome could accommodate several C*c* molecules. Data processing and analyses were carried out with the Nanoanalyze software (TA Instruments).

Cytochrome *c* oxidase assays

The ability of C*c* species to act as electron donors for cytochrome *c* oxidase (C*c*O) activity was tested in isolated complex IV and in mitochondria from *Saccharomyces cerevisiae*. Two yeast cell strains were used for mitochondria extraction, namely WT (BY4741; MATa; ura3Δ0; leu2Δ0; his3Δ1; met15Δ0) (WT_{mito}) and C*c*-deficient Y06846 (BY4741; MATa; ura3Δ0; leu2Δ0; his3Δ1; met15Δ0; YJR048w::kanMX4) (Δ*Cc*) strains. Two other yeast cell strains were likewise used for mitochondria extraction, namely WT (W303-1A; mata leu2 trp1 ura3 his3 ade2) (WT_{Rcf}) and Rcf-deficient RCF1::HIS3 RCF2::KAN (W303-1A; mata leu2 trp1 ura3 ade2) (ΔRcf1/2) strains. WT_{mito} and Δ*Cc* cells were grown in YPD medium (1% yeast extract, 2% peptone and 2% glucose), whereas WT_{Rcf} and ΔRcf1/2 cells were grown in YPD medium or YP-0.5% lactate medium supplemented with 2% galactose (YP-Gal), as described previously (38), to obtain mitochondria-enriched cells. In all cases, crude mitochondria were isolated as previously described (39) and stored at –80^{o}C in 0.6 M sorbitol, 20 mM K-MES buffer (pH 6.0). The C*c*O activity was measured spectrophotometrically (Beckman DU® 650 spectrophotometer) using the commercial C*c*O activity kit from Sigma®, according to the manufacturer's instructions. The kit uses a colorimetric assay based on observation of the decrease in absorbance at 550 nm caused by oxidation of ferro-C*c* to ferri-C*c* by C*c*O. The WT and Y48*p*CMF recombinant forms of

human C*c* herein used (rather than C*c* provided with the Sigma kit) were used. It was also tested that endogenous C*c* from WT_{mito}, WT_{Rcf} and ΔRcf1/2 mitochondria did not affect the C*c*O assay. To facilitate the interpretation of experimental findings, the relative C*c*O activities were represented upon normalization of the data obtained with Y48*p*CMF to those with WT C*c*. In experiments with HIGD1A/2A proteins, the reaction mixtures were incubated at 25 ºC for 30 min before running the assay. Oxygen consumption rates were measured with an Oxygraph system (Hansatech) in the presence of 1 mM sodium ascorbate. A control trace (C*c*O in the presence of sodium ascorbate) was subtracted from the experimental data.

Liposome preparation and binding experiments

In order to analyze the interaction of the reduced C*c* species with cardiolipin (CL), small unilamellar liposomes were prepared by sonication in 25 mM HEPES buffer (pH 7.4). Liposomes contained either DOPC and TOCL (4:1 ratio) or DOPC alone (manufactured by Avanti Polar Lipids®). The diameter of liposomes was 27.5 ± 10.8 nm, as inferred by Dynamic Light Scattering measurements. C*c*:liposome binding assays were performed by incubating the C*c* species with DOPC or TOCL/DOPC liposomes at different ratios (protein:lipids) for 1 h in 25 mM HEPES buffer (pH 7.4). The complexes were analyzed by electrophoretic mobility shift assay (EMSA). The samples were applied onto 0.8% agarose gel, and the electrophoresis was run for 90 min at 50 V in non-denaturing 35 mM HEPES buffer (pH 7.4). Gels were stained for protein detection with 0.25% Coomassie Brilliant Blue R-250 in 45% methanol and 10% acetic acid.

Peroxidase assays

Peroxidase assays of C*c*:liposomes were performed as previously described with minor modifications (40). TOCL/DOPC liposomes were incubated for 1 h at room temperature with

reduced C*c* (1 μM) in a 1:100 ratio (w/w) (protein:lipid) in 20 mM HEPES buffer (pH 7.4). After incubation, and immediately before starting the measurement, 2′,7′-dichlorofluorescin diacetate (H_2DCF) and H_2O_2 were added to the samples at 5 μM and 100 μM final concentrations, respectively. Increases in DCF fluorescence at 522 nm were recorded along 30 min upon excitation at 502 nm, with 5-nm slits, in a Cary Eclipse (Varian) fluorescence spectrophotometer. Basal peroxidase activity of C*c* in CL-free liposomes was used as control.

Caspase activation assays

In vitro activation of caspases was achieved as described previously with minor modifications (41). Human embryonic kidney 293 (HEK 293) cytoplasmic cell extract (100 μg), prepared as described previously (42), was incubated for 60 min at 37°C, in a total volume of 25 μL, with 25 mM KCl, 0.2 mM DTT, 0.2 mM dATP and human WT or Y48*p*CMF C*c* at a final concentration of 8 μM. After incubation, 180 μL of buffer A (10 mM HEPES buffer (pH 7.0) with 50 mM NaCl, 40 mM β-glycerophosphate, 2 mM $MgCl_2$, 5 mM EGTA, 0.1 mg mL^{-1} bovine serum albumin, and 0.1% (w/v) CHAPS), supplemented with 10 μM of acetyl-Asp-Glu-Val-Asp-7-amino-4-methylcoumarin (Ac-DEVD-AMC; a fluorescent substrate specific for caspases 3/7), was added to the reaction mixture. Fluorescence increases resulting from Ac-DEVD-AMC cleavage was rapidly determined in a Cary Eclipse (Varian) fluorescence spectrophotometer (optical slits of 2.5 nm), using an excitation wavelength of 360 nm and an emission wavelength of 460 nm. Data were the averages of at least three independent experiments.

Blue-native gel electrophoresis of protein complexes from yeast mitochondria

Fresh mitochondria (400 µg of protein) isolated from yeast cell extracts were permeabilized in 40 µL of solubilization buffer (30 mM HEPES buffer (pH 7.4), with 150 mM KOH-acetate, 10% glycerol and 1 mM PMSF) plus digitonin at a 4:1 (w:w) ratio of digitonin:protein. Samples were incubated on ice for 30 min, centrifuged for 30 s, and loaded onto NativePAGE Novex 3–12% Bis-Tris protein gel (1.0 mm, 15-well; Thermo Fisher Scientific, cat. No. BN2012BX10), following the manufacturer's instructions.

Antibodies

Mouse monoclonal anti-His_6 and anti-α-tubulin were obtained from Sigma-Aldrich (catalog numbers 11922416001 and T8328, respectively). Secondary horseradish peroxidase (HRP)-conjugated anti-mouse IgG was obtained from Sigma-Aldrich (catalog number A4416). Rabbit antibody against yeast C*c*, and mouse antibody again yeast COX II, were a gift from Dr. Carlos Santos-Ocaña. Rabbit antibodies against the C-terminal domains of yeast Rcf1 and Rcf2 were kindly provided by Prof. Peter Rehling. Rabbit antiserum against yeast Cc_1 was a gift from Prof. Nikolaus Pfanner. Rabbit anti-human C*c* serum was obtained by immunizing male rabbits with full-length recombinant C*c* suspended in a 0.85% NaCl solution. Secondary horseradish peroxidase (HRP)–conjugated anti-rabbit IgG was obtained from Sigma-Aldrich (catalog number A0545).

Western blot analysis

For immunoblot detection of yeast C*c*, Rcf1 and Rcf2 in mitochondria and human C*c* and α-tubulin in cytoplasmic fractions of HEK293 cells, protein quantification was first assessed using the Bradford protein assay (43). For immunodetection of Cc_1, COX II, Rcf1 and Rcf2 inside the respiratory supercomplexes, mitochondrial content were obtained after permeabilization and protein quantification by the Bradford protein assay (43). For

cytoplasmic cell extracts and mitochondria samples, 10–20 μg of proteins were resolved by β-dodecyl sulphate–polyacrylamide gel electrophoresis (SDS-PAGE). For supercomplexes analysis, 20-μg protein samples were loaded onto NativePAGE Novex 3–12% Bis-Tris protein gels (1.0 mm, 15-well; Thermo Fisher Scientific, catalog number BN2012BX10), which were further transferred to polyvinylidene fluoride (PVDF) membranes (EMD Millipore) using a Mini Trans-Blot electrophoretic transfer cell (Bio-Rad). Membranes were blocked in 5% nonfat dry milk in PBS with Tween-20 (TPBS) for cytoplasmic extracts and mitochondria, and in only TBS for supercomplex analyses. Immunoblots were performed with primary antibodies, and then HRP-conjugated secondary antibodies were used for detection. The immunoreactive bands were detected using Amersham ECL Plus Western Blotting Detection Reagents (GE Healthcare Life Sciences).

SUPPLEMENTARY TABLES

Table S1. **NMR experiments performed on reduced Y48*p*CMF C*c***

	Experiments	Magnetic Field
Backbone assignment	2D ^{1}H-^{15}N HSQC, 2D ^{1}H-^{13}C HSQC, 3D HNCA, 3D HNCACB, 3D CBCA(CO)NH, 3D HN(CA)CO and 3D HNCO.	700 MHz
Side-chain assignment	2D ^{1}H-^{13}C HSQC, 2D COSY, 3D HBHA(CO)NH and 3D HCCH-TOCSY.	700 MHz
	Aromatic 2D ^{1}H-^{13}C HSQC	500 MHz
Mobility analysis	^{15}N R_1, ^{15}N R_2 and steady-state {^{1}H}-^{15}N NOE	500 MHz
Distance constraints	2D ^{1}H-^{1}H NOESY, 3D ^{1}H-^{15}N NOESY-HSQC, 3D ^{1}H-^{13}C NOESY-HSQC	950 MHz
Heme assignments & constraints	2D COSY, 2D ^{1}H-^{15}N NOESY and ^{1}H-^{15}N EXSY	950 MHz
Amide hydrogen exchange	2D ^{1}H-^{15}N HSQC	700 MHz
Biomolecular interactions	2D ^{1}H-^{15}N HSQC	700 MHz

Table S2. NMR statistics of the Y48*p*CMF C*c* structure

NMR distance and dihedral constraints	
Distance constraints	
Total meaningful NOE	2,176
Intra-residue	360
Inter-residue	1,816
Sequential ($\|i - j\| = 1$)	763
Medium-range ($\|i - j\| \leq 5$)	539
Long-range ($\|i - j\| > 5$)	514
Total dihedral angle restraints	
ϕ	71
ψ	71
Structure statistics	
Violations	
Average target function	0.73 ± 0.18
Distance constraints (Å)	0.0059 ± 0.0014
Dihedral angle constraints (º)	0.3336 ± 0.0973
Max. distance constraint violation (Å)	0.29
Max. dihedral angle violation (º)	3.79
RMSD of minimized 20 conformers to the mean (Å)	
Backbone	0.89 ± 0.01
Heavy atoms	1.33 ± 0.24
Global RMSD of minimized 20 conformers (Å)	
Backbone	1.28 ± 0.30
Heavy atoms	1.91 ± 0.38
Ramachandram plot statistics from Procheck	
Residues in favoured regions (%)	98.80 ± 0.10
Residues in generously allowed regions (%)	1.00 ± 0.10
Residues in disallowed regions (%)	0.20 ± 0.10
Global quality	
Procheck G-factor (all dihedrals, raw score)	-0.436 ± 0.046
Verify 3D	0.432 ± 0.030
Prosall	0.578 ± 0.047
MolProbity Clashscore	2.564 ± 1.263
Number of close contacts	0
Deviations from ideal bond distance (Å)	0.013 ± 0.001

Table S3. EXAFS fits of the Y48*p*CMF C*c* structure

	Paths	σ^2_{path} (Å^2)	R (Å)	ΔE_0 (eV)
WT	N_{Pi}	0.0012 ± 0.0006	1.983 ± 0.008	0.5 ± 1.0
	N_{Iz}	0.0011	2.214	
	S	0.002 ± 0.002	2.26 ± 0.01	
	C_{Pi}	0.002 ± 0.001	2.98	
			3.02 ± 0.01	
			3.06	
	Pi Multiple	0.002		
Y48*p*CMF	N_{Pi}	0.003 ± 0.001	1.990 ± 0.001	0.4 ± 1.3
	N_{Iz}	0.0011	2.21	
	S	0.003 ± 0.002	2.25 ± 0.01	
	C_{Pi}	0.002 ± 0.001	2.99	
			3.03 ± 0.02	
			3.06	
	Pi Multiple	0.003		

*The amplitude reduction factor, S_0^2, was set to 1.0 for all fits. Δk_{WT} = 1.389 ─ 11.885 Å^{-1}; $\Delta k_{Y48pCMF}$ = 1.358 ─ 11.685 Å^{-1}; ΔR_{WT} = 1.15 ─ 2.95 Å; $\Delta R_{Y48pCMF}$ = 1.18 ─ 2.95 Å. Fit *R* factors: R_{WT} = 0.0043; $R_{Y48pCMF}$ = 0.0097.

Table S4. Comprehensive ^{15}N relaxation parameters of the WT and Y48*p*CMF C*c* species

	WT C*c*	Y48*p*CMF C*c*	Difference
R_1 (s^{-1})	2.26 ± 0.08	2.15 ± 0.07	0.11
R_2 (s^{-1})	8.53 ± 0.46	9.14 ± 0.48	0.61
R_2 / R_1	3.77 ± 0.23	4.25 ± 0.23	0.48
NOE ratio	0.80 ± 0.03	0.80 ± 0.02	0.00
τ_c (ns)	6.33 ± 0.02	6.96 ± 0.02	0.63

Table S5. Equilibrium and thermodynamic parameters for the interaction of WT and Y48*p*CMF C*c* at the two binding sites of C*c*$_1$, as determined by ITC

	***Proximal* site**				***Distal* site**				
Protein couple	K_{D1} (μM)	ΔH_1 (kcal/mol)	$-T\Delta S_1$ (kcal/mol)	ΔG_1 (kcal/mol)	K_{D2} (μM)	ΔH_2 (kcal/mol)	$-T\Delta S_2$ (kcal/mol)	ΔG_2 (kcal/mol)	***n***
C*c* WT$_{red}$/C*c*$_{1red}$[a,1]	11.5	11.7	–18.40	–6.70	54.0	10.5	–16.30	–5.80	2
C*c* Y48*p*CMF$_{red}$/C*c*$_{1red}$[a]	5.1	–1.8	–5.42	–7.22	230.0	4.4	–9.36	–4.96	2
C*c* WT$_{ox}$/C*c*$_{1ox}$[b]	1.9	6.2	–14.00	–7.80	110.0	1.1	–6.50	–5.40	2
C*c* Y48*p*CMF$_{ox}$/C*c*$_{1ox}$[b]	1.8	8.2	–16.03	–7.83	71.0	3.3	–8.96	–5.66	2
C*c* WT$_{ox}$/C*c*$_{1ox}$[c]	50.0	4.3	–10.16	–5.86	140.0	0.8	–6.05	–5.25	2
C*c* Y48*p*CMF$_{ox}$/C*c*$_{1ox}$[c]	12.0	1.4	–8.11	–6.71	140.0	1.3	–6.55	–5.25	2

Relative errors: K_D, 20%; ΔH and $-T\Delta S$, 5%; ΔG 2%

[1] = Ref. 3

[a] = pH 7.4

[b] = pH 5.8

[c] = pH 8.5

Table S6. Equilibrium and thermodynamic parameters for the interaction of WT and Y48*p*CMF C*c* at the two binding sites of bovine C*c*O, as determined by ITC

	***Proximal* site**				***Distal* site**				
Protein couple	K_{D1} (μM)	ΔH_1 (kcal/mol)	$-T\Delta S_1$ (kcal/mol)	ΔG_1 (kcal/mol)	K_{D2} (μM)	ΔH_2 (kcal/mol)	$-T\Delta S_2$ (kcal/mol)	ΔG_2 (kcal/mol)	***n***
C*c* WT_{red}/C*c*O_{red}[1]	0.03	–6.6	–3.7	–10.3	0.30	–5.4	–3.5	–8.9	2
C*c* Y48*p*CMF_{red}/C*c*O_{red}	2.10	–6.3	–1.4	–7.7	7.00	–30.0	23.0	–7.0	2

Relative errors: K_D, 20%; ΔH and $-T\Delta S$, 5%; ΔG, 2%

[1] = Ref. 3.

SUPPLEMENTARY FIGURES

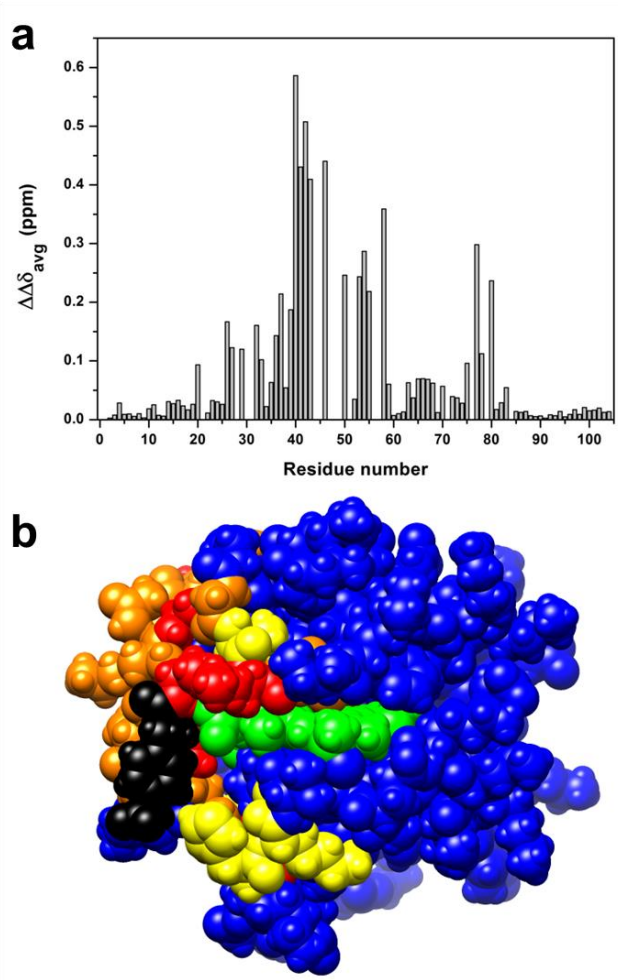

Figure S1. Chemical-shift differences between WT and Y48*p*CMF C*c*. (a) Plot of the chemical-shift differences between both C*c* species for backbone amides along their primary sequence. **(b)** The chemical shift differences are mapped on the Y48*p*CMF C*c* surface according to the degree of change. Residues are colored in yellow if the chemical-shift difference ranged between 0.1 and 0.2 ppm, and in red if the difference was greater than 0.2 ppm. Residues with undetectable backbone amide resonances in the ^{1}H-^{15}N HSQC spectrum of Y48*p*CMF C*c* but detectable in WT C*c* are colored in orange. *p*CMF48 and the heme group are given in black and green, respectively. Unaffected, unassigned and proline residues are in blue.

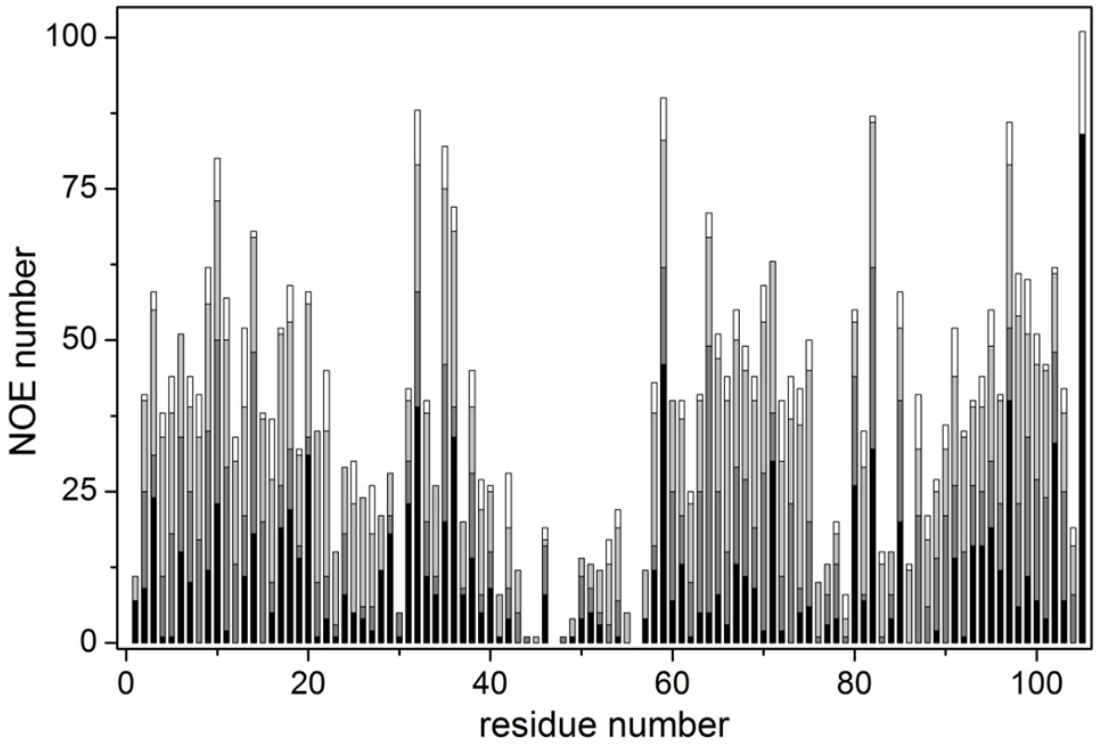

Figure S2. **Number of experimental meaningful NOEs per residue used for the structure calculation of Y48*p*CMF C*c*.** The color code for the NOE bars is: intra-residue, white; sequential, light gray; medium, gray; and long range, black. Residue 105 corresponds to the heme group.

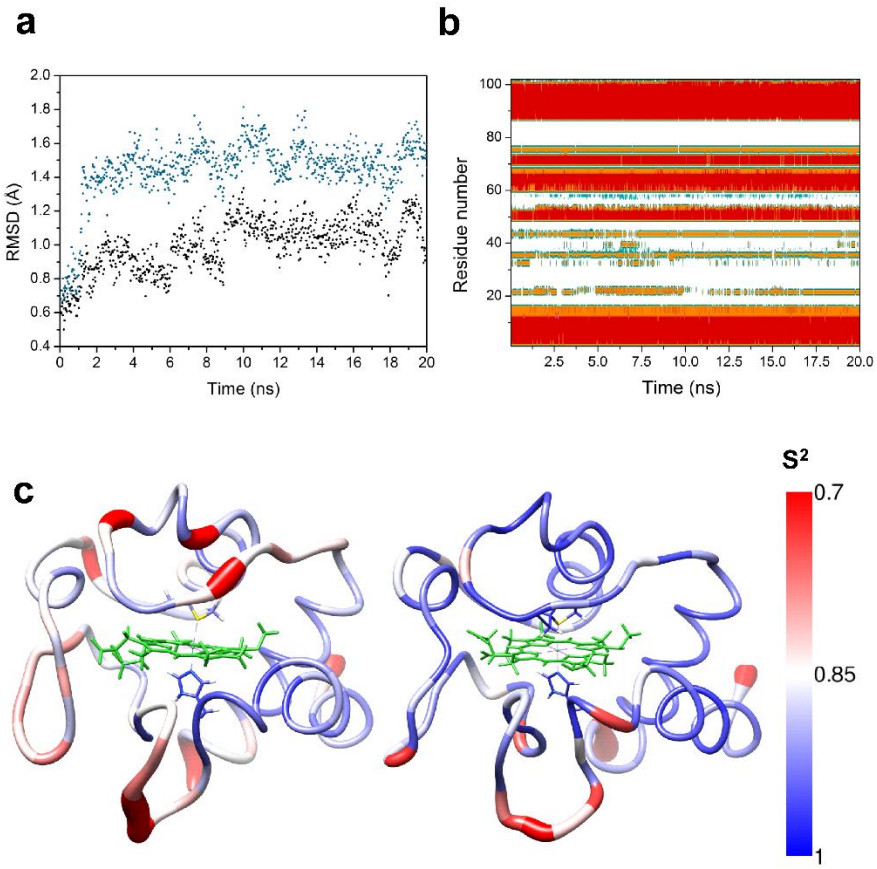

Figure S3. Molecular Dynamics simulations for the Y48*p*CMF variant and WT form of C*c*. (a) A non-restrained MD computation was performed to check the stability of conformers derived from the NMR structure of Y48*p*CMF C*c*. RMSD values are plotted along the full 20 ns trajectory, considering either residues away from the mutation surroundings (black) or the whole protein sequence (blue). **(b)** Time evolution of secondary structural elements along the MD trajectory represented in (**a**). The color code is as follows: α-helix, red; π-helix, orange; extended β-brand, blue; β-bridge, cyan; turn, yellow; and coil, white. **(c)** Comparison of S^2 order parameter values for Y48pCMF and WT C*c* obtained from MD computations. S^2 order parameter values per residue for Y48*p*CMF (*left*) and WT (*right*) C*c* are represented on their respective NMR ribbon structures using a blue-red scale (color key is shown). Heme atoms are in green. Heme axial ligands are also displayed. Internal mobility of alpha carbon atoms was calculated with the Amber software.

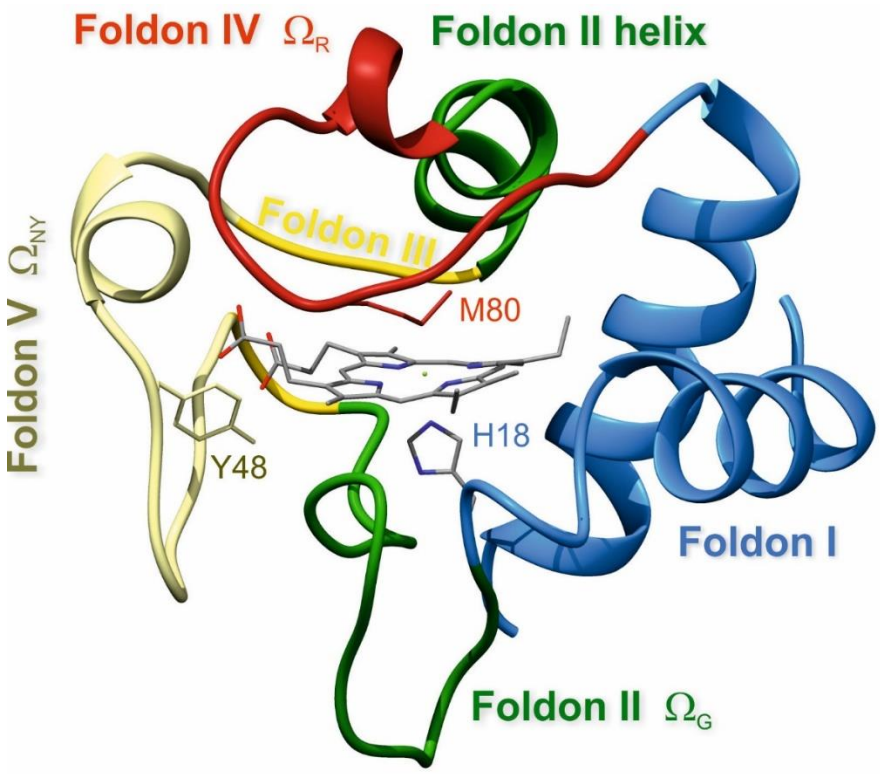

Figure S4: Folding units of WT C*c*. Ribbon diagram of human WT C*c* (PDB ID: 1J3S) (36), colored according to the foldon units schema by Maity and Eglander (44).

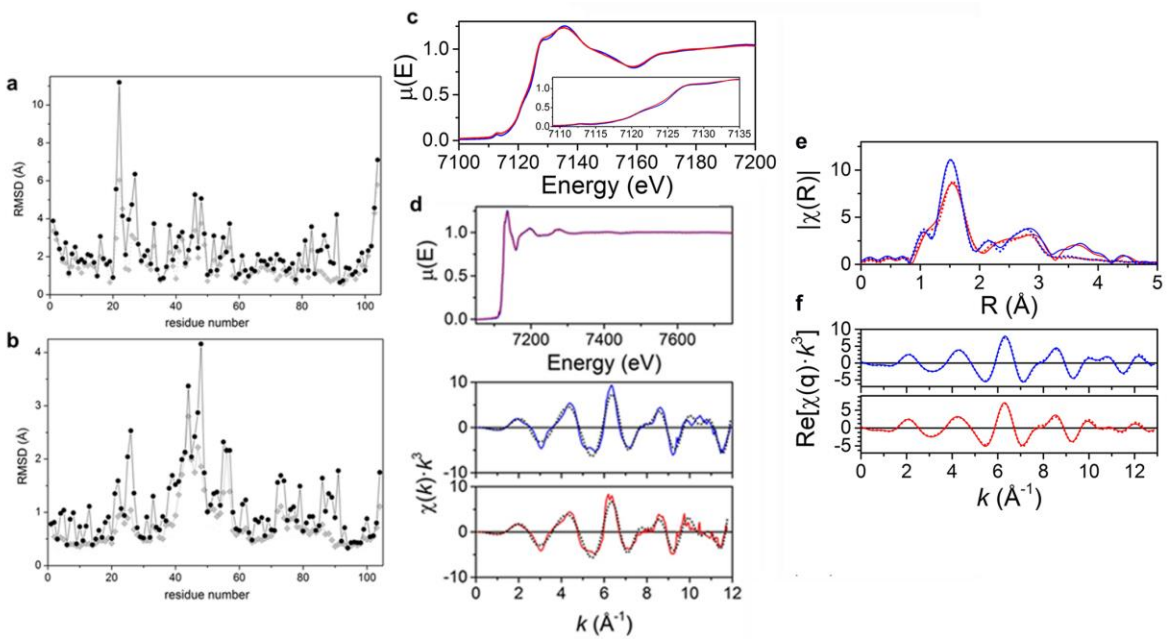

Figure S5. **NMR data in combination with XAS measurements. (a)** Per residue RMSD values between the first conformer of the NMR solution structures of WT C*c* (PDB ID: 1J3S) (36) and the refined lowest-TF Y48*p*CMF C*c*. Backbone and heavy atoms are represented as gray triangles and black circles, respectively. RMSD calculations were performed with the MOLMOL software (45). **(b)** Global RMSD values per residue of the best 20 conformers of Y48*p*CMF C*c* with respect to the mean structure. The color code is as in (**a**). **(c)** Overlay of the X-ray absorption near-edge structure (XANES) regions of the X-ray Absorption Spectra (XAS) spectra of reduced WT (blue) and Y48*p*CMF (red) C*c*. The *inset* displays an enlargement of the absorption edge. **(d)** Normalized XAS and Extended absorption fine Structure (EXAFS) waves of WT (blue) and Y48*p*CMF (red) C*c*. Black dots correspond to the best fits summarized in **Table S3**. **(e)** Modulus of the Fourier transforms of the EXAFS signals for the reduced WT (continuous line, blue) and Y48*p*CMF (continuous line, red) C*c* species. Dotted curves are the best fits of the experimental data carried out within the interval ΔR = 1.38–2.95 Å. **(f)** *q*-space, reverse Fourier transform of the experimental data (continuous lines) and best fits (dotted lines), following the same color-code as for **(e).**

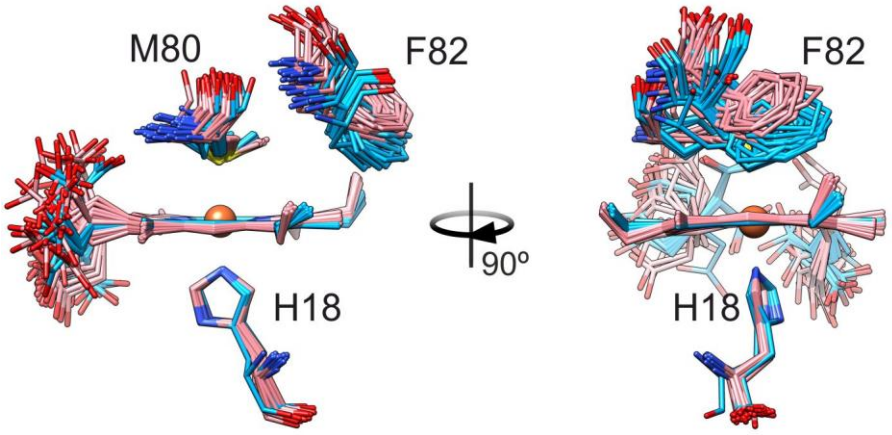

Figure S6. Relative orientation of Phe82 with respect to the heme moiety. The ensemble of the NMR structures from WT C*c* (PDB CODE: 1J3S) (36) and the Y48*p*CMF mutant (this work) are represented in sticks. Heavy atoms except carbons are in CPK colors, whereas carbons are colored in cyan and pink for the WT and mutant structures, respectively.

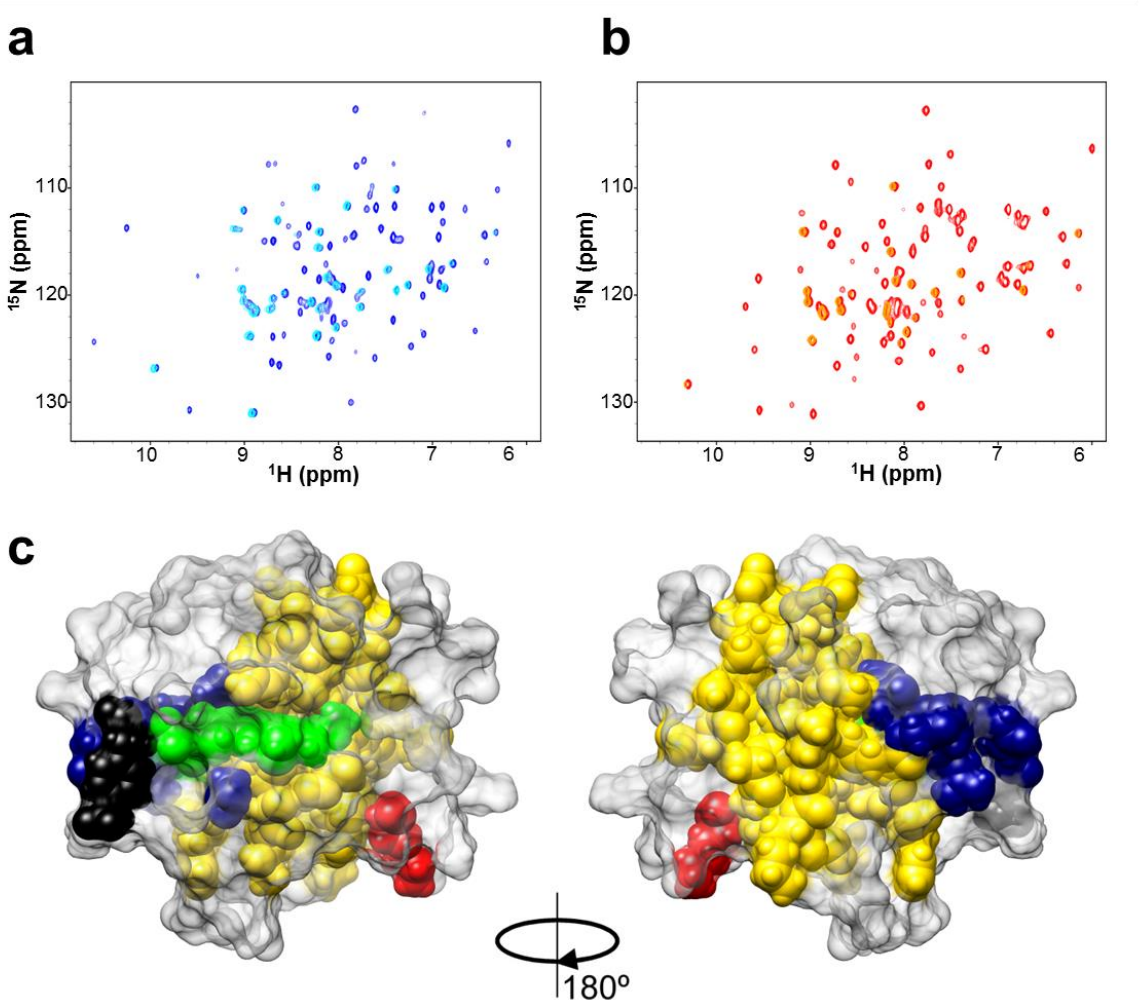

Figure S7. **Amide-hydrogen exchange experiments with WT and Y48*p*CMF C*c*. (a)** ^{1}H-^{15}N HSQC spectrum of WT C*c* recorded either in 95% H_2O and 5% D_2O (blue) or in 100% D_2O (cyan). **(b)** ^{1}H-^{15}N HSQC spectrum of Y48*p*CMF C*c* recorded either in 95% H_2O and 5% D_2O (red) or in 100% D_2O (gold). **(c)** Residues protected from amide-hydrogen exchange in both C*c* species are displayed in gold, those protected only in Y48*p*CMF C*c*, in red, and those protected only in WT C*c*, in blue. *p*CMF48 and the heme group are in black and green, respectively. The representation is projected on the Y48*p*CMF C*c* structure, whose surface is light gray.

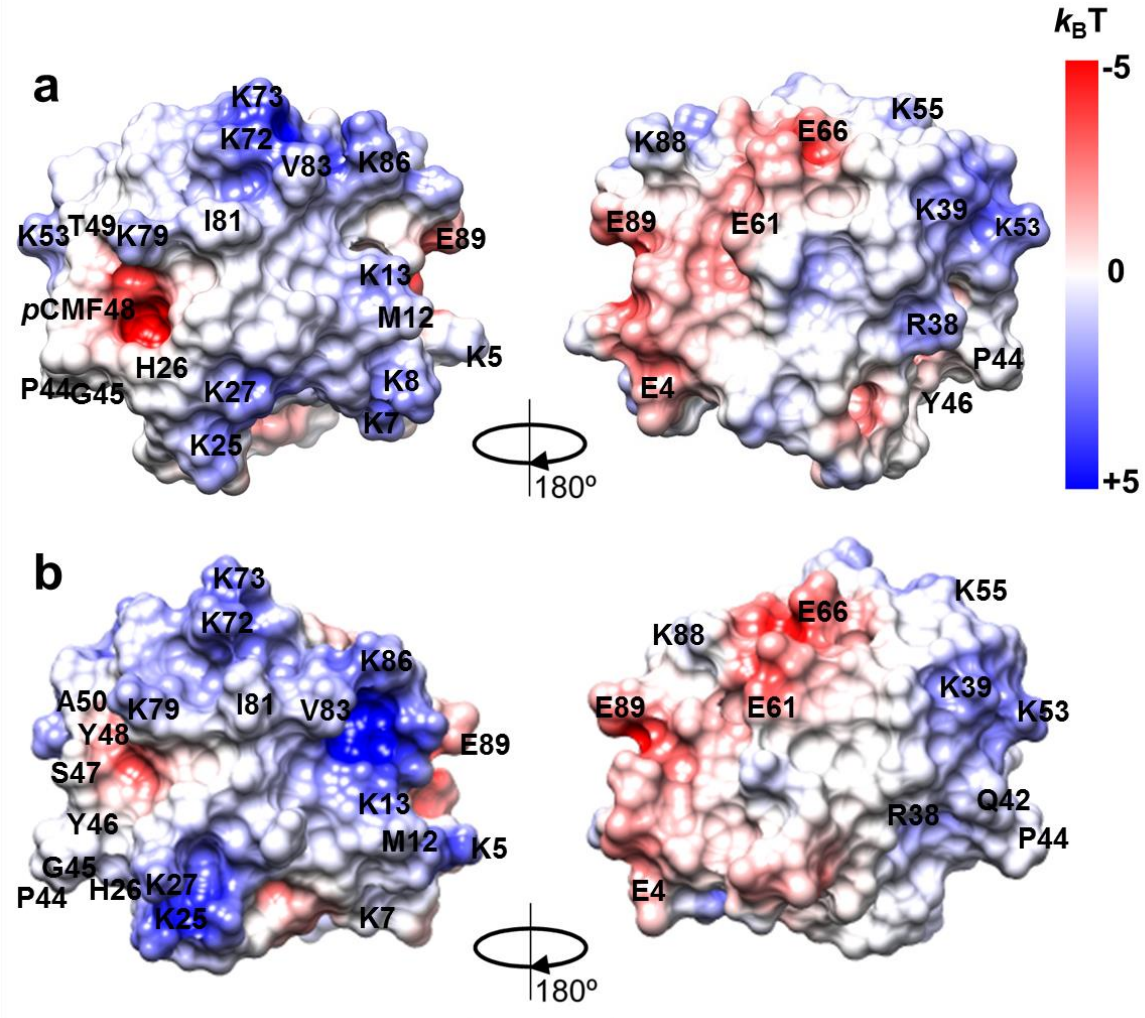

Figure S8. **(a**,**b) Surface electrostatic potentials of WT (a) and Y48*p*CMF (b) C*c* molecules.** Negatively and positively charged regions are depicted in red and blue, respectively. Simulations were performed with the DelPhi program (46) aided by Chimera (31), assuming an ionic strength of 250 mM. The color scale ranges from –5 (red) to +5 (blue) k_BT. Some residues were labelled to better show the orientation of both C*c* species. The PDB file 1J3S was used for the WT C*c* structure.

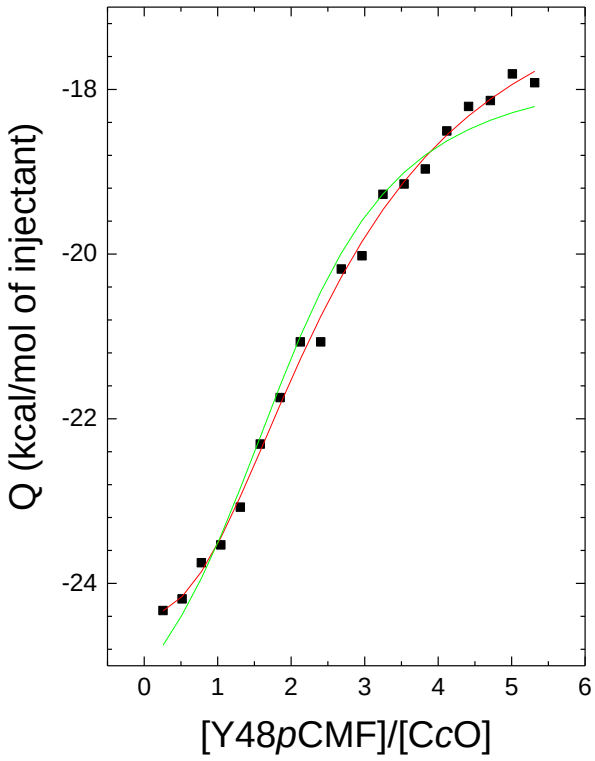

Figure S9. **ITC isotherms for the interaction of the Y48*p*CMF C*c* mutant with C*c*O.** Solid squares represent experimental data, which are fitted to a 2:1 model using either two identical (green) or different (red) K_D values.

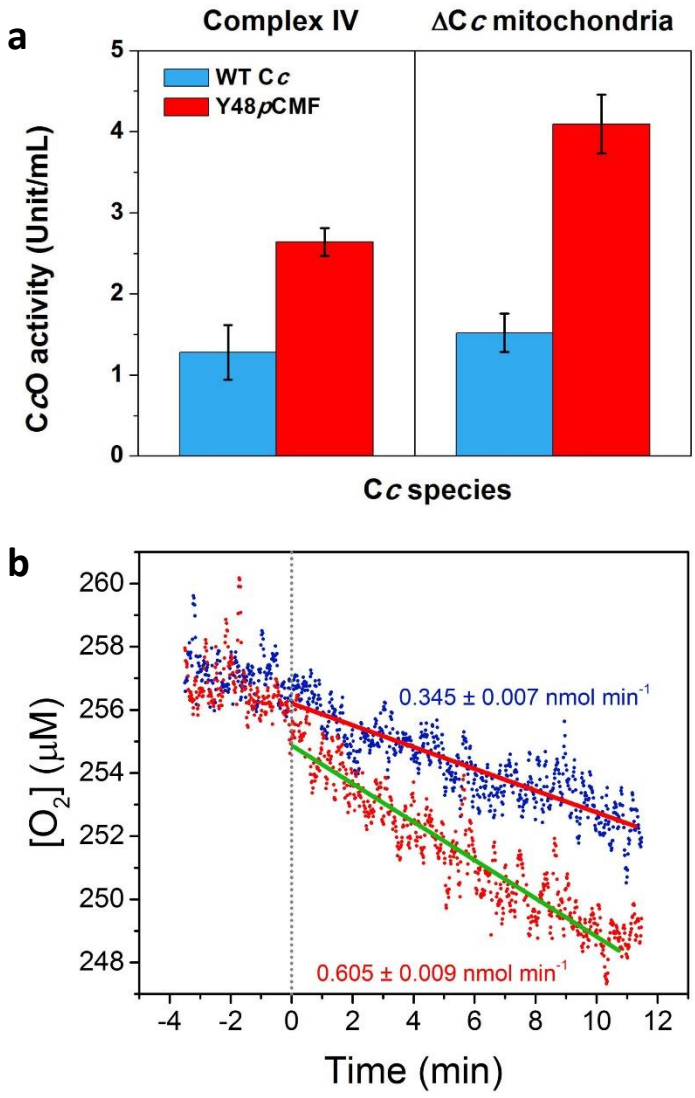

Figure S10. **Standard C*c*O assays. a)** Data in Figure 5a without normalization. C*c*O activities were measured by monitoring the absorption changes at 550 nm, as reported under Supplementary Methods. Activity units are μmol C*c* min^{-1}. **b)** Oxygen consumption under the experimental conditions used for the spectrophotometric assays. 1 mM sodium ascorbate was added to the reaction mixture. A control trace obtained with sodium ascorbate was subtracted from the experimental data, which are in blue and red for WT and mutant C*c*, respectively. The resulting oxygen consumption rates were calculated from the respective linear fit slopes.

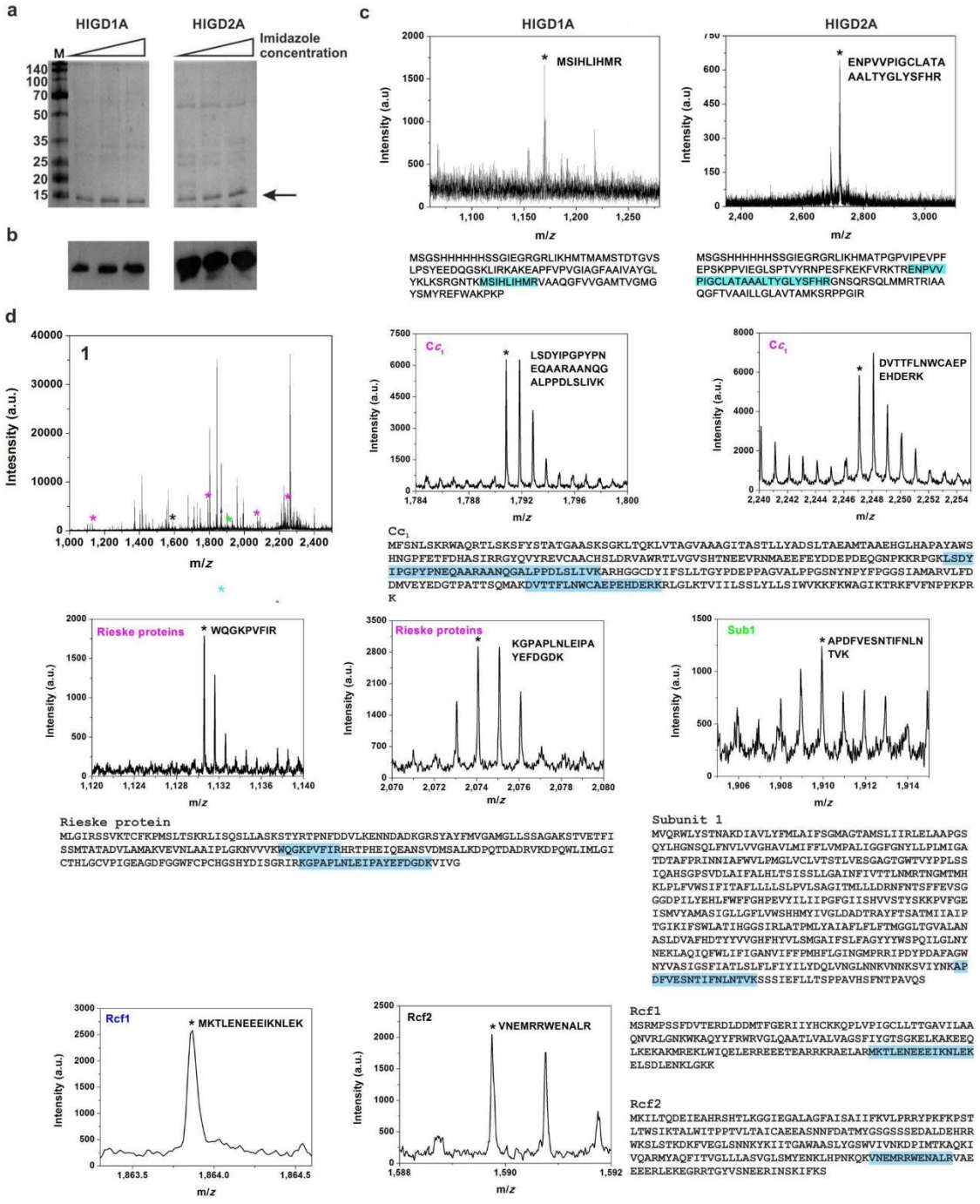

Figure S11. **HIGD proteins**. **(a)** SDS-PAGE of purified HIGD1A and HIGD2A His-tagged proteins after applying an imidazole gradient. M, molecular weight markers. The arrow points to the bands corresponding to HIGD proteins. **(b)** Western blot analysis using an antibody against His-tag to identify HIGD1A and HIGD2A following Ni-column purification. **(c)** Trypsin digestion of HIGD proteins followed by matrix-assisted laser desorption ionization with time-

of-light (MALDI-TOF) analysis. **(d)** Tryptic digestion of proteins from BN-PAGE bands followed by MALDI-TOF/TOF and highlighted by asterisks in Figure 5D. Specifically, the data presented here correspond to the upper band in YP-Gal in Figure 5D. The expected tryptic masses clearly matched the calculated values, with 0.5 Da tolerance. The sequence coverage of these fragments is shaded in cyan.

REFERENCES

1. Xie J, Supekova L, Schultz PG (2007) A genetically encoded metabolically stable analogue of phosphotyrosine in *Escherichia coli*. *ACS Chem Biol* 2: 474-478.
2. Guerra-Castellano A, *et al.* (2015) Mimicking tyrosine phosphorylation in human cytochrome *c* by the evolved tRNA synthetase technique. *Chem Eur J* 21: 15004-15012.
3. Moreno-Beltrán B, *et al.* (2015) Respiratory complexes III and IV can each bind two molecules of cytochrome *c* at low ionic strength. *FEBS Lett* 589: 476-483.
4. Moreno-Beltrán B, *et al.* (2014) Cytochrome c_1 exhibits two binding sites for cytochrome *c* in plants. *Biochim Biophys Acta – Bioenerg* 1837: 1717-1729.
5. Kelly SM, Jess TJ, Price NC (2005) How to study proteins by circular dichroism. *Biochim Biophys Acta – Proteins Proteomics* 1751: 119-139.
6. Sreerama N, Woody RM (2000) Estimation of protein secondary structure from circular dichroism spectra: comparison of CONTIN, SELCON, and CDSSTR methods with an expanded reference set. *Anal Biochem* 282: 252-260.
7. Greenfield NJ (2007) Using circular dichroism spectra to estimate protein secondary structure. *Nat Protoc* 1: 2876-2890.
8. Zuiderweg ER, Fesik SW (1988) Heteronuclear 3-dimensional NMR spectroscopy. A strategy for the simplification of homonuclear two-dimensional NMR spectra. *J Magn Reson* 78: 588-593.
9. Grzesiek S, Bax A (1993) Amino acid type determination in the sequential assignment procedure of uniformly $^{13}C/^{15}N$-enriched proteins. *J Biomol NMR* 3: 185-204.
10. Kay LE, Xu G, Singer AU, Muhandiram DR, Forman-Kay JD (1993) A gradient-enhanced HCCH-TOCSY experiment for recording side-chain ^{1}H and ^{13}C correlation in H_2O samples of proteins. *J Magn Reson* 101: 333-337.
11. Piotto M, Saudek V, Sklenar V (1991) Gradient-tailored excitation for single-quantum NMR spectroscopy of aqueous solutions. *J Biomol NMR* 2: 661-665.

12. Marion D, *et al.* (1989) Overcoming the overlap problem in the assignment of ^{1}H NMR spectra of larger proteins by use of three-dimensional heteronuclear ^{1}H-^{15}N Hartmann-Hahn-multiple quantum coherence and nuclear Overhauser-multiple quantum coherence spectroscopy: application to interleukin 1β. *Biochemistry* 28: 6150-6156.
13. Marion D, Kay LE, Sparks SW, Torchia DA, Bax A (1989). Three-dimensional heteronuclear NMR of nitrogen-^{15} labeled proteins. *J Am Chem Soc* 111: 1515-1517.
14. Zuiderweg ER, Fesik SW (1989) Heteronuclear three-dimensional NMR spectroscopy of the inflammatory protein C5a. *Biochemistry* 28: 2387-2391.
15. Kay LE, Torchia DA, Bax A (1989) Backbone dynamics of proteins as studied by ^{15}N inverse detected heteronuclear NMR spectroscopy: application to staphylococcal nuclease. *Biochemistry* 28: 8972-8979.
16. Blackledge M, Cordier F, Dosset P, Marion D (1998) Precision and uncertainty in the characterization of rotational diffusion from heteronuclear relaxation data. *J Am Chem Soc* 120: 4538-4539.
17. Dosset P, Hus JC, Blackledge M, Marion D (2000) Efficient analysis of macromolecular rotational diffusion from heteronuclear relaxation data. *J Biomol NMR* 16: 23-28.
18. Goddar TD, Kneller DG (2001) SPARKY 3, University of California, San Francisco, CA, USA.
19. Keller R (2004) The computer aided resonance assignment tutorial, 1st edn. CANTINA Verlag, Goldau, Switzerland.
20. Baistrocchi P, Banci L, Bertini I, Turano P (1996) Three-dimensional solution structure of *Saccharomyces cerevisiae* reduced iso-1-cytochrome *c*. *Biochemistry* 35: 13788-13796.
21. Bartels C, Xia TH, Billeter M, Guntert P, Wuthrich K (1995) The program XEASY for computer-supported NMR spectral analysis of biological macromolecules. *J Biomol NMR* 6: 1-10.

22. Güntert P, Mumenthaler C, Wüthrich K (1997) Torsion angle dynamics for NMR structure calculation with the new program Dyana1. *J Mol Biol* 273: 283-298.
23. Bartalesi I, Bertini I, Rosato A (2003) Structure and dynamics of reduced *Bacillus pasteurii* cytochrome *c*: oxidation state dependent properties and implications for electron transfer processes. *Biochemistry* 42: 739-745.
24. Banci L, *et al.* (1997) Solution structure of oxidized *Saccharomyces cerevisiae* iso-1-cytochrome *c*. *Biochemistry* 36: 8992-9001.
25. Assfalg M, *et al.* (2002) A quick solution structure determination of the fully oxidized double mutant K9-10A cytochrome c_7 from *Desulfuromonas acetoxidans* and mechanistic implications. *J Biomol NMR* 22: 107-122.
26. Duan Y, *et al.* (2003) A point-charge force field for molecular mechanics simulations of proteins based on condensed-phase quantum mechanical calculations. *J Comput Chem* 24: 1999-2012.
27. Case DA, *et al.* (2006) AMBER 9 University of California, San Francisco.
28. Andersen HC (1980) Molecular dynamics simulations at constant pressure and/or temperature. *J Chem Phys* 24: 1999-2012.
29. Ryckaert JP, Ciccotti G, Berendsen HJC (1977) Numerical integration of the cartesian equations of motion of a system with constraints: Molecular dynamics of *n*-Alkanes. *J Comp Phys* 23: 327-341.
30. Autenrieth F, Tajkhorshid E, Baudry J, Luthey-Schulten Z (2004) Classical force field parameters for the heme prosthetic group of cytochrome *c*. *J Comput Chem* 25: 1613-1622.
31. Pettersen EF, *et al.* (2004) UCSF Chimera - A visualization system for exploratory research and analysis. *J Comput Chem* 25: 1605-1612.
32. Bhattacharya A, Tejero R, Montelione GT (2007) Evaluating protein structures determined by structural genomics consortia. *Proteins* 66: 778-795.

33. Doreleijers JF, *et al.* (2012) CING: an integrated residue-based structure validation program suite. *J Biomol NMR* 54: 267-283.
34. Ravel B, Newville M (2005) ATHENA, ARTEMIS, HEPHAESTUS: data analysis for X-ray absorption spectroscopy using IFEFFIT. *J Synchrotron Rad* 12: 537-541.
35. Rajagopal BS, *et al.* (2013) The hydrogen-peroxide-induced radical behaviour in human cytochrome *c*-phospholipid complexes: implications for the enhanced pro-apoptotic activity of the G41S mutant. *Biochem J* 456: 441-452.
36. Jeng WY, Chen CY, Chang HC, Chuang WJ (2002) Expression and characterization of recombinant human cytochrome *c* in *E. coli*. *J Bioenerg Biomembr* 34: 423-431.
37. Serpas L, Milorey B, Pandiscia LA, Addison AW, Schweitzer-Stanner R (2016) Autoxidation of reduced horse heart cytochrome c catalyzed by cardiolipin-containing membranes. *J Phys Chem B* 120: 12219-12231.
38. Strogolova V, Furness A, Robb-McGrath M, Garlich J, Stuart RA (2012) Rcf1 and Rcf2, members of the hypoxia-induced gene 1 protein family, are critical components of the mitochondrial cytochrome bc_1-cytochrome *c* oxidase supercomplex. *Mol Cell Biol* 32: 1363-1373.
39. Padilla-López S. *et al.* (2009) Genetic evidence for the requirement of the endocytic pathway in the uptake of coenzyme Q6 in *Saccharomyces cerevisiae*. *Biochim Biophys Acta – Biomembr* 1788: 1238-1248.
40. Belikova NA, *et al.* (2006) Peroxidase activity and structural transitions of cytochrome *c* bound to cardiolipin-containing membranes. *Biochemistry* 45: 4998-5009.
41. Rodríguez-Roldán V, García-Heredia JM, Navarro JA, De la Rosa MA, Hervás M (2008) Effect of nitration on the physicochemical and kinetic features of wild-type and monotyrosine mutants of human respiratory cytochrome *c*. *Biochemistry* 47: 12371-12379.

42. Pecina P, *et al.* (2010) Phosphomimetic substitution of cytochrome *c* tyrosine 48 decreases respiration and binding to cardiolipin and abolishes ability to trigger downstream caspase activation. *Biochemistry* 49: 6705-6714.
43. Bradford MM (1976) A rapid and sensitive method for the quantitation of microgram quantities of protein utilizing the principle of protein-dye binding. *Anal Biochem* 72: 248-254.
44. Maity H, Maity M, Englander SW (2004) How cytochrome *c* folds, and why: submolecular foldon units and their stepwise sequential stabilization. *J Mol Biol* 34: 223-233.
45. Koradi R, Billeter M, Wüthrich K (1996) MOLMOL: a program for display and analysis of macromolecular structures. *J Mol Graph* 51: 29-32.
46. Nicholls A, Honig B (1991) A rapid finite difference algorithm, utilizing successive overrelaxation to solve the Poisson–Boltzmann equation. *J Comput Chem* 12: 435-445.